GUIDANCE AND CONTROL OF UNMANNED AIRSHIPS FOR WAYPOINT NAVIGATION IN THE PRESENCE OF WIND

by

GHASSAN M.ATMEH

Presented to the Faculty of the Graduate School of
The University of Texas at Arlington in Partial Fulfillment
of the Requirements
for the Degree of

MASTER OF SCIENCE IN AEROSPACE ENGINEERING

THE UNIVERSITY OF TEXAS AT ARLINGTON

May 2012

To my parents, Nadia Zash and Mohammad Atmeh

ACKNOWLEDGEMENTS

First and foremost I would like to thank God for blessing me with the ability to work hard and produce this thesis. I would like to acknowledge my supervising professor Dr. Kamesh Subbarao for his guidance throughout my masters degree, his patience during frustrating times, and his constant motivation for research. I would also like to thank Dr. Don Wilson for his academic advising, Dr. Haiying Huang for inspiring me to be an engineering researcher during my first semester of graduate school, Dr. Atilla Dogan and Dr. David Hullender for taking the time to serve as my thesis committee members. My thanks also extends to all my teachers, in school and during my pursuit of an undergraduate degree in Jordan, with special thanks to Dr. Feras Darwish for encouraging me to pursue a graduate degree.

My deep gratitude also goes to my colleagues at the Aerospace Systems Laboratory at the University of Texas at Arlington, thanks to Laura Suarez Henderson, Pavan Kumar Nuthi, Mousumi Ahmed, Divya Bhatia, Alok Rege, and Marcin Brodecki for all the invaluable insight each of them provided. I would also like to acknowledge my dear friend Zeaid Hassan for his support, my brother and two sisters for being the best family anyone can ever ask for.

My deepest gratitude and love however go to my parents; I thank them for thier unconditional support during my studies, without them I would not be the man I am today, I owe it all to them.

April 19, 2012

ABSTRACT

GUIDANCE AND CONTROL OF UNMANNED AIRSHIPS FOR WAYPOINT NAVIGATION IN THE PRESENCE OF WIND

Ghassan M.Atmeh, MS

The University of Texas at Arlington, 2012

Supervising Professor: Kamesh Subbarao

Airships are a specific class of Lighter-Than-Air (LTA) vehicles. These vehicles achieve lift mainly through buoyancy; the usually ellipsoidal shaped hull contains a lifting gas such as helium, which produces the required lift though air displacement. Due to this method of operation an airship has the ability to conduct low-power hover, which makes it ideal for applications requiring hovering over long periods of time such as surveillance, terrain mapping, meteorology and GPS. In such applications the conventional fixed wing unmanned aircraft is less suitable.

The work presented in this thesis deals with designing a controller that is capable of navigating an airship through a series of waypoints. A guidance algorithm provides commands to the controller based on vehicle and waypoint positions (two approaches were considered). A novel implementation of the extended Kalman filter (EKF) provides the required states and wind speed estimates to increase the control systems robustness to wind.

Translational and rotational kinematics and dynamics for the AS500 unmanned airship are developed using classical mechanics principles, resulting in a nonlinear

model. Airship dynamics differ strongly from conventional aircraft dynamics for they exhibit virtual mass and virtual inertia effects, the aerodynamic model incorporated in this work take into account these effects as the airship moves through air.

The developed model is trimmed at two points, one for a straight and level flight the other for a level turn. These trim points are then incorporated in the linearization of the airship model, which results in a twelve-state, linear, state-space model. The linear model acquired is then used to design an Linear Quadratic Regulator (LQR) control law, a Linear Quadratic Integral (LQI) control law, and a gain scheduling law, which allow the airship to navigate through several waypoints. Two waypoint navigation laws are developed to generate command signals to the proposed controllers. The results from both cases are compared under specified wind conditions.

A novel implementation of the Extended Kalman filter (EKF) is employed to estimate the airship entire state vector, angular rates measurement bias, and wind speeds with only two sensors available; a global positioning system (GPS) and inertial measurement unit (IMU) sensor. It is shown that the inclusion of the estimated wind speeds enhances the robustness of the track following guidance law to wind.

The nonlinear model, proposed LQR and LQI controller, along with the guidance laws, and Extended Kalman filter are implemented to simulate the flight of the unmanned airship through a series of waypoints, in the presence of a wind field generated from an exponentially correlated wind model.

TABLE OF CONTENTS

LIST OF ILLUSTRATIONS

LIST OF TABLES

CHAPTER 1

INTRODUCTION

1.1 Background and Motivation

The dream of flight has always accompanied man throughout history. From Leonardo da Vincis designs, to Otto Lilienthals gliders , and all the way to the Wright brothers flight in Kitty Hawk, North Carolina, the dream of flight always captured mans imagination. The dream of a controlled, powered flight was first realized by the invention of the airship, where it is claimed that Jean-Baptiste Meusnier proposed a design of an ellipsoidal airship in 1748 [1]; the design incorporated a rudder, elevator and three large airscrews; however, it lacked a lightweight, powerful engine. Henri Giffard was the first person to equip an airship with steam-engine technology successfully flying his airship 17 miles in 1852, with a single propeller driven by a three horsepower engine [2]. The golden age of the airship began with the launch of German Luftschiff Zeppelin in 1900 but sadley ended in the tragic Hindenburg incident in 1937. During that period there were many designs that came out in the United States and Britain as well. Despite the demise of the golden age of airships, in the past decade interest in them has grown due to the advancement in technology such as thermal analysis, control system design, computational fluid dynamics, and optimal design. The fact that evolving new demands, which cannot be satisfied with conventional aircraft, are being imposed on the aeronautics community, has also sparked the interest in airships [3]. Therefore, addressing the issue of analyzing the dynamics of such vehicles along with implementing control methodologies that insure peak performance and safety, is necessary for the continued advancement of the airship technology.

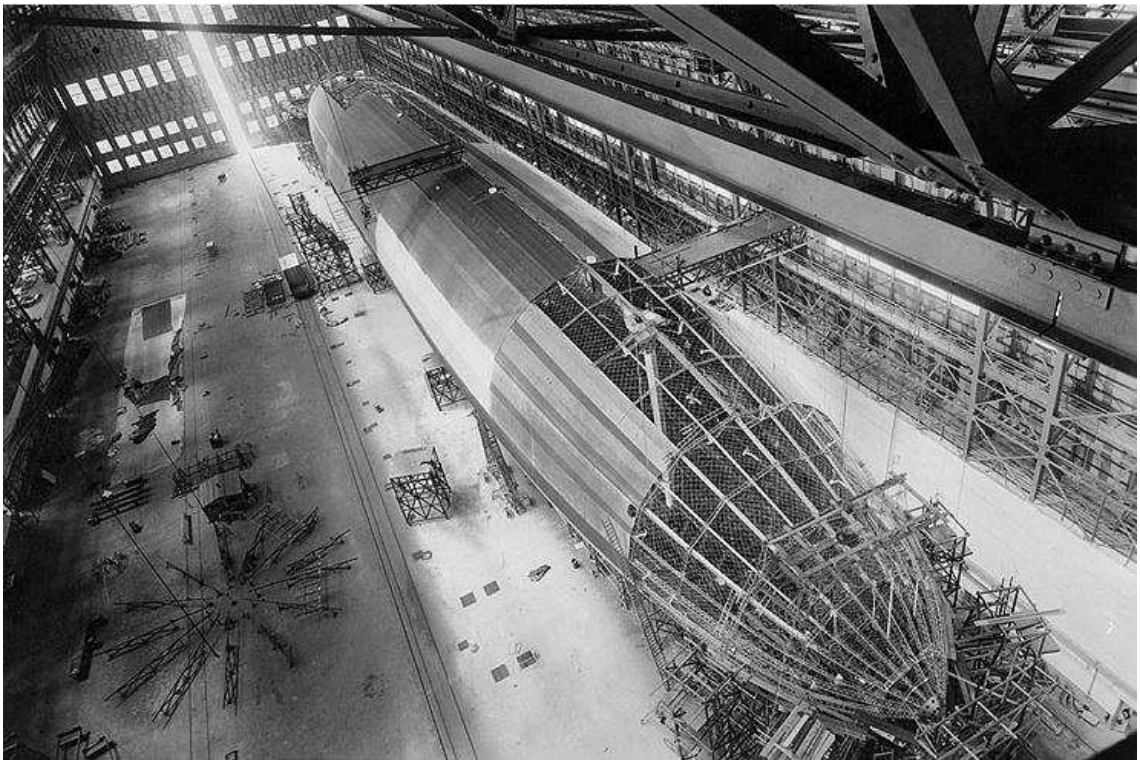

Figure 1.1. USS Shenandoah Under construction, courtesy U.S. Naval Historical Center.

Airships generally comprise of a hull, usually of ellipsoidal shape, a gondola, and aerodynamic tail fins. The hull houses a low-density lifting gas, such as helium, to achieve lift mainly through buoyancy. Fluid statics dictates that an object which is less dense than the fluid in which it is immersed, experiences a force proportional to the volume of the displaced fluid and in the opposite direction of its weight. Airships utilize gases that are less dense than air to generate such force for means of flight, this force is called the static lift. Due to this, airship dynamics are substantially different from conventional aircraft dynamics, with significant effects from added mass and added inertia, and a much higher sensitivity to wind [4]. Added mass and inertia effects are changes in the dynamics of the airship due to mass and inertia of air in which the it is flying. This is experienced by all aircraft, however in heavier-than-

Figure 1.2. A blimp from Airship Management Services, courtesy of AirshipManagement Services, Inc.

air flight, the mass and inertia of air are negligible when compared to that of the aircraft, in lighter-than-air flight such as airship flight they have a too profound of an effect on airship dynamics that they cannot be neglected. Due to this method of operation, airships have the ability to hover. This ability transforms airships into data acquisition platforms [5] ideal for applications such as surveillance, terrain mapping, climate research, inspection of man-made structures and GPS. In such applications the conventional unmanned aircraft is not a applicable.

There are three main categories for airship classification [6], all based on structural aspects; rigid airships, non-rigid airships, and semi-rigid airships. Rigid airships employ rigid-framed hulls to keep their shape, and contain multiple balloons filled

with the lifting gas. An example of rigid airships is the USS Shenandoah shown in Figure.1.1. Non-rigid airships, or blimps, keep their shape based on pressure difference between the inside lifting gas and the outside atmosphere. Figure.1.2 shows an example of a non-rigid airship (blimp). Semi-rigid airships also rely on pressure difference to maintain shape but incorporate some rigid parts to allow load distribution.

In light of all above mentioned, airship dynamics analysis and control is an interesting Field of study, therefore, in this thesis the focus will be on unmanned airship dynamics; analysis, estimation and control. The motivation behind this work is the need to control an unmanned airship under real life disturbances, i.e wind. Airships high sensitivity to wind originates from the fact that they have large wetted areas and depend on light gases for lift, and due to this method of lift generation they have special attributes. A major attribute is long endurance hover; this can transform airships to low cost data reception and transmission platforms. One example is the utilization of airships instead of space satellites for GPS applications. This would reduces the cost substantially, since there is no need for a rocket launch to get the airship into position, in addition if any malfunction should occur the airship can always land and be maintains, unlike satellites where a space mission would be conducted, and many more reasons. Therefore the need to control unmanned airships is vital to the advancement of technologies that can inhibit their utilization in such applications.

1.2 Thesis Outline

The goal of this thesis is to simulate the ability to control an unmanned airship to navigate its way through a series of waypoints, in the presence of wind. It is required that the airship visit all waypoints in the order they are given. In chapter 2 the dynamics and kinematics equations of an airship which, include the added mass

and inertia effects along with wind effects, are derived. These equations will be used to create a computer simulation of the airship flight. Chapter 3 deals with linearizing the developed nonlinear airship equations of motion, and utilizing the linear model for the design of an LQR full-state-feedback controller and an LQI controller. The purpose of the controllers is to fly the airship through a series of waypoints based on commands generated by a navigation algorithm. Two guidance laws are developed and utilized, a comparison in the results is shown to study the difference in the logic of both laws. An Novel Extended Kalman filter (EKF) is also designed and implemented in chapter 4 to estimate the required states for feedback control. The EKF is also responsible for estimating the wind speeds to enhance the performance of the controller. This is done by feeding the estimated wind speeds to the navigation algorithm which generates commands, that account for the presence of wind, to the controller, this makes the system more robust to wind.

CHAPTER 2

KINEMATICS AND DYNAMICS

The motion of an object in 3-dimensional space can be described, mathematically, in many ways. As customary to aerospace engineering applications, the dynamics and kinematics of the airship in 3-dimensional space are obtained using the principles of classical mechanics. Newton's second law on the rate of change of linear momentum is used to derive the equations for translational dynamics, while Euler's second law on angular momentum enables the derivation of the equations for rotational dynamics. Before diving into the detailed derivation, the airship adopted for this work will be introduced followed by some mathematical concepts needed for the equations derivation.

2.1 Airship Major Components

The airship selected for the work presented in this thesis is the AS500 airship [7, 8, 9, 10]. The AS500 has a main hull engulfing the lifting gas and aerodynamic tail fins incorporating control surfaces for stability and control. A main propeller, capable of tilting for thrust vectoring, is positioned below the hull along the gondola. A tail propeller is mounted to act as an aid in heading control. Figure 2.1 illustrates the main components of the AS500.

2.2 Mathematical Preliminaries

In order to acquire the equations that describe the airship motion some mathematical concepts are needed to aid in the process. The required concepts are revised

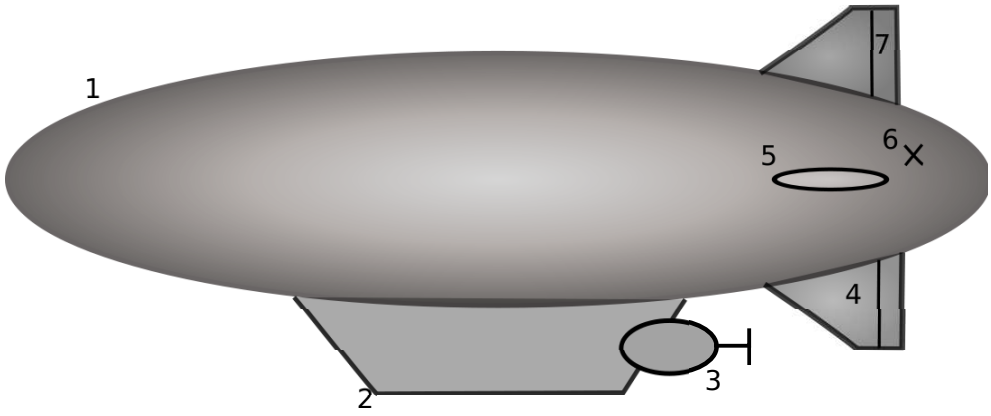

(1) Airship hull (2) Gondola (3) Main propeller
(4) Tail fin (5) Tail fin (6) Tail propeller
(7) Aerodynamic control surface

Figure 2.1. Schematic drawing showing the main components of the AS500 airship - not to scale.

in this section. Throughout this thesis the following notation will be adopted if not otherwise stated; vectors will be denoted by boldface font lowercase letters and matrices will be expressed in boldface font uppercase letters.

1. Vector triple product

$$\mathbf{a} \times (\mathbf{b} \times \mathbf{c}) = (\mathbf{a}.\mathbf{c})\mathbf{b} - (\mathbf{a}.\mathbf{b})\mathbf{c} \tag{2.1}$$

2. Vector quadruple product

$$\mathbf{a} \times (\mathbf{b} \times (\mathbf{c} \times \mathbf{d})) = (\mathbf{b}.\mathbf{d})\mathbf{a} \times \mathbf{c} - (\mathbf{b}.\mathbf{c})\mathbf{a} \times \mathbf{d} \tag{2.2}$$

3. Vectors scalar product via their representations

$$\mathbf{a}.\mathbf{b} = \mathbf{a}^T\mathbf{b} \tag{2.3}$$

4. Vectors vector product via their representations

$$\mathbf{a} \times \mathbf{b} = -[\mathbf{a}]_\times \mathbf{b} \tag{2.4}$$

where $\mathbf{a} = [a_1\ a_2\ a_3]^T$ and $[\mathbf{a}]_\times$ is the skew-symmetric cross-product matrix and is calculated as follows

$$[\mathbf{a}]_\times = \begin{bmatrix} 0 & a_3 & -a_2 \\ -a_3 & 0 & a_1 \\ a_2 & -a_1 & 0 \end{bmatrix}$$

5. Order of cross product

$$[\mathbf{a}]_\times \mathbf{b} = -[\mathbf{b}]_\times \mathbf{a} \tag{2.5}$$

6. Vectors product manipulation

$$\mathbf{a}^T \mathbf{bc} = \mathbf{ca}^T \mathbf{b} \tag{2.6}$$

7. The transport theorem

$$\dot{\mathbf{a}} = \frac{d\mathbf{a}}{dt}|_I + \boldsymbol{\omega}_{BI} \times \mathbf{a} \tag{2.7}$$

8. Other required equalities

$$(\mathbf{a}^T \mathbf{b})[\mathbf{a}]_\times = -[\mathbf{b}]_\times \mathbf{a}\mathbf{a}^T \tag{2.8}$$

$$[\boldsymbol{R_{12}}\mathbf{a}]_\times = \boldsymbol{R_{12}}[\mathbf{a}]_\times \boldsymbol{R_{12}}^T \tag{2.9}$$

where $\boldsymbol{R_{12}}$ is the rotation matrix from coordinate frame 1 to coordinate frame 2. The proofs for equations 2.8 and 2.9 are available in reference [11]

2.3 Assumptions

In order to derive the mathematical formulation for the airship equations of motion the following assumptions are stated:

- The airship is a rigid body; relative motion between volume elements of the airship is nonexistent.

- The airship has a fixed mass, and its center of mass is at a fixed location, i.e. no fuel or other mass is being introduced or exhausted from the airship.
- The airship center of volume is at a fixed location.
- The airship is at a neutral buoyancy state, i.e. the lift generated by the buoyancy force is equal to the airship weight.
- The earth is flat, nonrotating and is an approximate inertial frame.
- The airships body frame is located at a fixed geometric location, the nose. This assumption allows for a more general form of the equations of motion to be derived, for it can, if required, accommodate the movement of the center of mass or center of volume of the airship in future studies.

2.4 Translational Motion

The science of flight mechanics [12] is utilized to derive the equations of motion in this and subsequent section based on previous published equations of motion for an airship [9, 10], which were derived based on an extensive derivation for the equations of motion for an aircraft in an aerial refueling scenario [11]. The derivation is presented here for clarity and completion.

2.4.1 Translational kinematics

The airship motion in the inertial frame is the sum of the airship motion relative to the atmosphere and the atmospheres inertial motion.

$$\dot{\mathbf{r}}_a = \boldsymbol{R}_{IB}^T \mathbf{V} + \mathbf{W} \tag{2.10}$$

where $\boldsymbol{R}_{IB}$ is the rotation matrix from inertial frame to body frame, $\mathbf{r_a}$ is the position vector of the airships body frame origin, expressed in the inertial frame, $\mathbf{V}$ is the vector of airship velocity relative to the atmosphere expressed in the body frame, and $\mathbf{W}$ is

the atmosphere inertial velocity vector expressed in the inertial frame. All the vector components are expressed below.

$$\mathbf{r}_a = [x\ y\ z]^T$$

$$\mathbf{W} = [W_x\ Wy\ Wz]^T$$

$$\mathbf{V} = [u\ v\ w]^T$$

The rotation matrix from inertial frame to body frame is constructed based on the 3-2-1 Euler angle rotation sequence, the matrix elements are shown below where c and s denote cosine and sine respectively and ϕ, θ, and ψ are the bank, pitch, and yaw angles respectively.

$$\boldsymbol{R}_{IB} = \begin{bmatrix} c(\theta)c\psi & c(\theta)s(\psi) & -s(\theta) \\ -c(\phi)s(\psi) + s(\phi)s(\theta)c(\psi) & c(\phi)c(\psi) + s(\phi)s(\theta)s(\psi) & s(\phi)c(\theta) \\ s(\phi)s(\psi) + c(\phi)s(\theta)c(\psi) & -s(\phi)c(\psi) + c(\phi)s(\theta)s(\psi) & c(\phi)c(\theta) \end{bmatrix}$$

2.4.2 Translational dynamics

Newtons second law of motion states that the sum of forces acting at a point is equal to the rate of change of linear momentum. Based on the constant mass assumption made in section 2.3, the rate of change of linear momentum of the airship is equal to the mass multiplied by the acceleration of the center of mass expressed as follows

$$\sum \mathbf{F} = M\ddot{\mathbf{r}}_{cm} \tag{2.11}$$

with M is the scalar mass of the airship, vector $\mathbf{r}_{cm}$ is the inertial position of the airship center of mass expressed in the inertial frame. This vector is calculated based on vector addition of the inertial position vector of the airships body frame origin $\mathbf{r}_a$, expressed in the inertial frame, and the center of mass position vector relative to

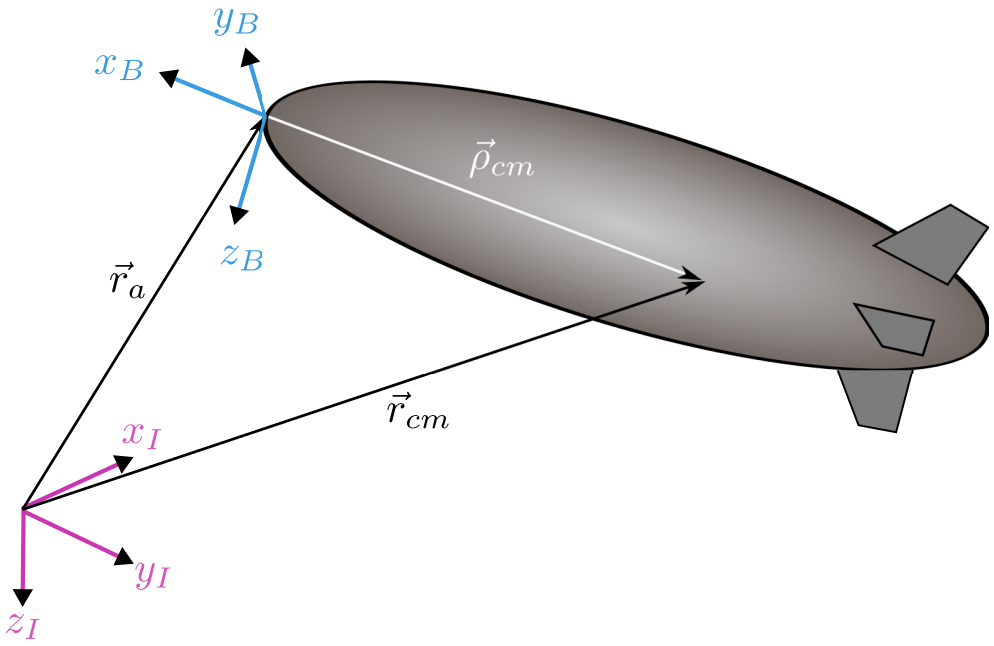

Figure 2.2. Graphical representation of position vectors required for equations of motion derivation.

the body frame $\boldsymbol{\rho}_{cm}$, expressed in the body frame. Figure 2.2 provides a graphical representation of these vectors.

$$\mathbf{r}_{cm} = \mathbf{r}_a + \boldsymbol{\rho}_{cm} \tag{2.12}$$

substituting equation 2.12 into equation 2.11 yields equation 2.13.

$$\sum \mathbf{F} = M(\ddot{\mathbf{r}}_a + \ddot{\boldsymbol{\rho}}_{cm}) \tag{2.13}$$

further substituting equation 2.10 into equation 2.13 and expressing all the vectors in the body frame gives

$$\sum \mathbf{F} = M\boldsymbol{R}_{IB}\dot{\boldsymbol{R}}_{IB}^{T}\mathbf{V} + M\dot{\mathbf{V}} + M\boldsymbol{R}_{IB}\dot{\mathbf{W}} + M\ddot{\boldsymbol{\rho}}_{cm} \tag{2.14}$$

Examining the last term on the right-hand side of equation 2.14 and utilizing the transport theorem from section 2.2. According to the theorem the following holds true

$$\dot{\boldsymbol{\rho}}_{cm} = \frac{d\boldsymbol{\rho}_{cm}}{dt}|_I + \boldsymbol{\omega}_{BI} \times \boldsymbol{\rho}_{cm} \tag{2.15}$$

where $\frac{d\boldsymbol{\rho}_{cm}}{dt}|_I = 0$ and $\boldsymbol{\omega}_{BI}$ is the airship angular velocity vector with respect to the inertial frame expressed in the body frame as $\boldsymbol{\omega}_{BI} = [p\ q\ r]^T$. This follows that

$$\ddot{\boldsymbol{\rho}}_{cm} = \dot{\boldsymbol{\omega}}_{BI} \times \boldsymbol{\rho}_{cm} + \boldsymbol{\omega}_{BI} \times \boldsymbol{\omega}_{BI} \times \boldsymbol{\rho}_{cm} \tag{2.16}$$

applying the cross-product matrix formulation and cross product properties discussed in section 2.2 to equation 2.16 results in

$$\ddot{\boldsymbol{\rho}}_{cm} = [\boldsymbol{\rho_{cm}}]_\times \dot{\boldsymbol{\omega}}_{BI} + [\boldsymbol{\omega_{BI}}]_\times^2 \boldsymbol{\rho}_{cm} \tag{2.17}$$

substituting equation 2.17 into equation 2.14 shows that

$$\sum \mathbf{F} = M\boldsymbol{R}_{IB}\dot{\boldsymbol{R}}_{IB}^T\mathbf{V} + M\dot{\mathbf{V}} + M\boldsymbol{R}_{IB}\dot{\mathbf{W}} + M[\boldsymbol{\rho}_{cm}]_\times\dot{\boldsymbol{\omega}}_{BI} + M[\boldsymbol{\omega}_{BI}]_\times^2\boldsymbol{\rho}_{cm} \tag{2.18}$$

recall from section 2.2 that $\dot{\boldsymbol{R}}_{IB} = [\boldsymbol{\omega_{BI}}]_\times \boldsymbol{R}_{IB}$ therefore

$$\dot{\boldsymbol{R}}_{IB}^T = -\boldsymbol{R}_{IB}^T[\boldsymbol{\omega_{BI}}]_\times \tag{2.19}$$

substituting equation 2.19 into equation 2.18 and rearranging yields

$$\sum \mathbf{F} = M(-[\boldsymbol{\omega_{BI}}]_\times\mathbf{V} + \dot{\mathbf{V}} + \boldsymbol{R}_{IB}\dot{\mathbf{W}} + [\boldsymbol{\rho_{cm}}]_\times\dot{\boldsymbol{\omega}}_{BI} + [\boldsymbol{\omega_{BI}}]_\times^2\boldsymbol{\rho}_{cm}) \tag{2.20}$$

The forces acting on the airship include aerodynamic, propulsive, gravitational, and buoyancy. All are to be discussed later in this chapter.

2.5 Rotational Motion

2.5.1 Rotational kinematics

The rotational kinematics or attitude kinematics can be expressed by the rate of change of the Euler angles. This is done by mapping the body angular velocity to

the inertial frame based on the rotation sequence, the sequence adopted here is the 3-2-1 sequence or yaw-pitch-roll sequence and the governing equation is

$$\dot{\mathbf{\Omega}} = \mathbf{\Gamma}(\mathbf{\Omega})\boldsymbol{\omega}_{BI} \tag{2.21}$$

where $\mathbf{\Omega} = [\phi\ \theta\ \psi]^T$ and $\mathbf{\Gamma}(\mathbf{\Omega})$ is shown below

$$\mathbf{\Gamma}(\mathbf{\Omega}) = \begin{bmatrix} 1 & \sin(\phi)\tan(\phi) & \cos(\phi)\tan(\phi) \\ 0 & \cos(\phi) & -\sin(\phi) \\ 0 & \sin(\phi)\sec(\theta) & \cos(\phi)\sec(\theta) \end{bmatrix}$$

2.5.2 Rotational dynamics

Euler's second law states that the rate of change of angular momentum about a point is equal to the sum of moments acting on that point. The sum of moments acting on the airship center of mass in the inertial frame is obtained from the following expression

$$\sum \mathbf{M}_I = \mathbf{r}_{cm} \times M\ddot{\mathbf{r}}_{cm} \tag{2.22}$$

the sum of moments on the airship in the body frame however reads as

$$\sum \mathbf{M}_B = \sum \mathbf{M}_I - \mathbf{r}_a \times \sum \mathbf{F} \tag{2.23}$$

from translational dynamics $\mathbf{r}_a \times \sum \mathbf{F} = \mathbf{r}_a \times M\ddot{\mathbf{r}}_{cm}$, and as established previously $\ddot{\mathbf{r}}_{cm} = \ddot{\mathbf{r}}_a + \ddot{\boldsymbol{\rho}}_{cm}$ therefore the following holds

$$\sum \mathbf{M}_B = \sum \mathbf{M}_I - \mathbf{r}_a \times M(\ddot{\mathbf{r}}_a + \ddot{\boldsymbol{\rho}}_{cm}) \tag{2.24}$$

substituting the value of the moment in equation 2.22 and the value of $\mathbf{r}_{cm}$ gives

$$\sum \mathbf{M}_B = (\mathbf{r}_a + \boldsymbol{\rho}_{cm}) \times M(\ddot{\mathbf{r}}_a + \ddot{\boldsymbol{\rho}}_{cm}) - \mathbf{r}_a \times M(\ddot{\mathbf{r}}_a + \ddot{\boldsymbol{\rho}}_{cm}) \tag{2.25}$$

which simplifies to

$$\sum \mathbf{M}_B = \boldsymbol{\rho}_{cm} \times M(\ddot{\mathbf{r}}_a + \ddot{\boldsymbol{\rho}}_{cm}) \tag{2.26}$$

the values of $\mathbf{r}_a$ from equation 2.10 and $\ddot{\boldsymbol{\rho}}_{cm}$ from equation 2.17 substituted into equation 2.26 along with expressing all vectors in the body frame gives

$$\begin{aligned}\sum \mathbf{M}_B =&\boldsymbol{\rho}_{cm} \times M(-[\boldsymbol{\omega_{BI}}]_\times \mathbf{V} + \dot{\mathbf{V}} + \boldsymbol{R}_{IB}\dot{\mathbf{W}})... \\ &+ \boldsymbol{\rho}_{cm} \times M(\dot{\boldsymbol{\omega}}_{BI} \times \boldsymbol{\rho}_{cm}) + \boldsymbol{\rho}_{cm} \times M(\boldsymbol{\omega}_{BI} \times \boldsymbol{\omega}_{BI} \times \boldsymbol{\rho}_{cm})\end{aligned} \tag{2.27}$$

from the triple cross product identity the second term on the right-hand side of equation 2.27 can be expressed as

$$\begin{aligned}\boldsymbol{\rho}_{cm} \times M(\dot{\boldsymbol{\omega}}_{BI} \times \boldsymbol{\rho}_{cm}) =&M[(\boldsymbol{\rho}_{cm}.\boldsymbol{\rho}_{cm})\dot{\boldsymbol{\omega}}_{BI} - (\boldsymbol{\rho}_{cm}.\dot{\boldsymbol{\omega}}_{BI})\boldsymbol{\rho}_{cm}] \\ =&[M(\boldsymbol{\rho}_{cm}^T\boldsymbol{\rho}_{cm})\boldsymbol{I}_{3\times3} - (\boldsymbol{\rho}_{cm}\boldsymbol{\rho}_{cm}^T)]\dot{\boldsymbol{\omega}}_{BI}\end{aligned} \tag{2.28}$$

similarly the third term on the right-hand side of equation 2.27 can be expressed as follows based on vector and matrix properties introduced in section 2.2

$$\begin{aligned}\boldsymbol{\rho}_{cm} \times M(\boldsymbol{\omega}_{BI} \times \boldsymbol{\omega}_{BI} \times \boldsymbol{\rho}_{cm}) =&M\boldsymbol{\rho}_{cm} \times [(\boldsymbol{\omega}_{BI}.\boldsymbol{\rho}_{cm})\boldsymbol{\omega}_{BI} - (\boldsymbol{\omega}_{BI}.\boldsymbol{\omega}_{BI})\boldsymbol{\rho}_{cm}] \\ =&M(\boldsymbol{\rho}_{cm}^T\boldsymbol{\omega}_{BI})\boldsymbol{\rho}_{cm} \times \boldsymbol{\omega}_{BI} \\ =&- M(\boldsymbol{\rho}_{cm}^T\boldsymbol{\omega}_{BI})[\boldsymbol{\rho_{cm}}]_\times\boldsymbol{\omega}_{BI} \\ =&- M[\boldsymbol{\omega_{BI}}]_\times(\boldsymbol{\rho}_{cm}\boldsymbol{\rho}_{cm}^T)\boldsymbol{\omega}_{BI} \\ =&- [\boldsymbol{\omega_{BI}}]_\times([M(\boldsymbol{\rho}_{cm}^T\boldsymbol{\rho}_{cm})\boldsymbol{I}_{3\times3} - (\boldsymbol{\rho}_{cm}\boldsymbol{\rho}_{cm}^T)]\boldsymbol{\omega}_{BI} \\ &- M(\boldsymbol{\rho}_{cm}^T\boldsymbol{\rho}_{cm})\boldsymbol{\omega}_{BI}) \\ =&- [\boldsymbol{\omega_{BI}}]_\times([M(\boldsymbol{\rho}_{cm}^T\boldsymbol{\rho}_{cm})\boldsymbol{I}_{3\times3} - (\boldsymbol{\rho}_{cm}\boldsymbol{\rho}_{cm}^T)]\boldsymbol{\omega}_{BI})\end{aligned} \tag{2.29}$$

where $[M(\boldsymbol{\rho}_{cm}^T\boldsymbol{\rho}_{cm})\boldsymbol{I}_{3\times3} - (\boldsymbol{\rho}_{cm}\boldsymbol{\rho}_{cm}^T)]$ is the mathematical definition of the inertia matrix $\boldsymbol{I}_M$, substituting equations 2.28 and 2.29 into equation 2.27

$$\sum \mathbf{M}_B = -M[\boldsymbol{\rho_{cm}}]_\times(-[\boldsymbol{\omega_{BI}}]_\times \mathbf{V} + \dot{\mathbf{V}} + \boldsymbol{R}_{IB}\dot{\mathbf{W}}) + \boldsymbol{I}_M\dot{\boldsymbol{\omega}}_{BI} - [\boldsymbol{\omega_{BI}}]_\times\boldsymbol{I}_M\boldsymbol{\omega}_{BI} \tag{2.30}$$

The moments acting on the airship include aerodynamic, propulsive, gravitational, and buoyancy moments. All are to be discussed in the following section.

2.6 Forces and Moments

2.6.1 Aerodynamics

Over the past century, airship aerodynamics have been the subject of study for many aerodynamicists and engineers [13, 14, 15, 16, 17]. In the past four years different methods have been applied to derive an aerodynamics model for airships, analytical [1] and numerical [18]. However, to acquire a high fidelity aerodynamics model wind tunnel tests are required [19]. To make an operational airship, it is necessary to provide control surfaces and propulsion devices [10]. Each of these items experiences individual drag when mounted to the hull due to the hull flow field. The control surfaces alter the force and moment coefficients, therefore, they are used to stabilize the airship. The gondola introduces asymmetry in the geometry of the vehicle and influences all the forces. The aerodynamic model developed in [4] based on the method outlined in [17] and was implemented in many technical publications on simulation and control of airship dynamics [9, 20, 21, 22, 23].

The aerodynamic model adopted for the work presented in this thesis is based on published data where the aerodynamic force and moment coefficients as a function of control surface deflection, angle of attack and angle of side-slip are derived from wind tunnel experiments. The reader is referred to ref.[10] for more detail. The aerodynamics force on the airship can be expressed as:

$$\mathbf{F}_A = \mathbf{F}_0 + \boldsymbol{F_1}\dot{\mathbf{V}} + \boldsymbol{F_2}\dot{\boldsymbol{\omega}}_{BA} \tag{2.31}$$

where F_1 and F_2 are the virtual mass matrices which are a contribution of the displacement of the air medium to the overall linear momentum change of a system

moving through it, $\mathbf{F}_0$ is the main aerodynamic force vector in the body frame and can be expressed as

$$\mathbf{F}_0 = \begin{bmatrix} F_{x_B} \\ F_{y_B} \\ F_{z_B} \end{bmatrix} = \begin{bmatrix} \frac{1}{2}\rho_{air}||\mathbf{V}||^2 S_{ref} C_T \\ \frac{1}{2}\rho_{air}||\mathbf{V}||^2 S_{ref} C_L \\ \frac{1}{2}\rho_{air}||\mathbf{V}||^2 S_{ref} C_N \end{bmatrix} - \boldsymbol{D_u} \begin{bmatrix} \mathbf{V} \\ \boldsymbol{\omega}_{BA} \end{bmatrix} \tag{2.32}$$

C_T, C_L, C_N are the body frame X-direction, Y -direction, and Z-direction aerodynamic force coefficients, S_{ref} is the reference surface area of the airship hull, and $\boldsymbol{D}_u$ is the translational portion of the Coriolis-centrifugal coupling matrix, and ρ is the air density [10].

$$\mathbf{M}_A = \mathbf{M}_0 + \boldsymbol{M_1}\dot{\boldsymbol{\omega}}_{BA} + \boldsymbol{M_2}\dot{\mathbf{V}} \tag{2.33}$$

where M_1 and M_2 are the virtual inertia matrices which are a contribution of the displacement of the air medium to the overall angular momentum change of a system moving through it, $\mathbf{M}_0$ is the main aerodynamic moment vector in the body frame and can be expressed as

$$\mathbf{M}_0 = \begin{bmatrix} M_{x_B} \\ M_{y_B} \\ M_{z_B} \end{bmatrix} = \begin{bmatrix} \frac{1}{2}\rho_{air}||\mathbf{V}||^2 S_{ref} L_{ref} C_l \\ \frac{1}{2}\rho_{air}||\mathbf{V}||^2 S_{ref} L_{ref} C_m \\ \frac{1}{2}\rho_{air}||\mathbf{V}||^2 S_{ref} L_{ref} C_n \end{bmatrix} - \boldsymbol{D_\omega} \begin{bmatrix} \mathbf{V} \\ \boldsymbol{\omega}_{BA} \end{bmatrix} \tag{2.34}$$

M_1 and M_2 are the virtual inertia matrices which are a contribution of the displacement of the air medium to the overall angular momentum change of a system moving through it. C_l, C_m, C_n are the body frame x-direction, y-direction, and z-direction aerodynamic moment coefficients, L_{ref} is the reference length of the airship hull,and $\boldsymbol{D}_\omega$ is the rotational portion of the Coriolis-centrifugal coupling matrix.

2.6.2 Propulsion

The AS500 airship has two sources of thrust, the main propeller and the tail propeller. The main propeller has a tilt capability that enables it to produce thrust

in the body frame x and z directions by rotating at an angle γ_{T_m}. The tail propeller only produces thrust in the y-direction of the body frame. The two vectors can be expressed in the body frame as

$$\mathbf{T}_m = \begin{bmatrix} T_m \cos(\gamma_{T_m}) \\ 0 \\ -T_m \sin(\gamma_{T_m}) \end{bmatrix} \tag{2.35}$$

$$\mathbf{T}_t = \begin{bmatrix} 0 \\ T_t \\ 0 \end{bmatrix} \tag{2.36}$$

where T_m and T_t are the magnitude of the main and tail thrust respectively.

The moment due to the the propulsive forces acting on the airship in the body frame can be calculated by multiplying the thrust vectors of both the main propeller and the tail propeller by the location of each in the body frame and adding the results, this is shown as

$$\mathbf{M}_p = \boldsymbol{\rho}_{T_m} \times \mathbf{T}_m + \boldsymbol{\rho}_{T_t} \times \mathbf{T}_t \tag{2.37}$$

where $\boldsymbol{\rho}_{T_m}$ and $\boldsymbol{\rho}_{T_t}$ are the position vectors of the main and tail propeller respectively in the body frame.

2.6.3 Buoyancy and weight

The buoyancy force generated by the lifting gas acts in an opposite direction to the weight. They both are represented in the inertial frame as one buoyancy-weight vector $\mathbf{F}_{bg_I} = [0 \;\; 0 \;\; (F_g - F_b)]^T$, therefore to express the buoyancy-weight force vector in the body frame it is premultiplied by the rotation matrix as follows

$$\mathbf{F}_{bg_B} = \boldsymbol{R}_{IB} \mathbf{F}_{bg_I} \tag{2.38}$$

and the moment due to the buoyancy force can be expressed as the product of the location of the center of volume and the buoyancy force vector in the body frame.

$$\mathbf{M}_{bouy} = \boldsymbol{\rho}_{cv} \times \boldsymbol{R}_{IB}\mathbf{F}_{b_I} \tag{2.39}$$

where $\boldsymbol{\rho}_{cv}$ is the location of the center of volume in the body frame, expressed in the body frame and $\mathbf{F}_{b_I}$ is the buoyancy force acting on the airship expressed in the inertial frame. the moment due to the weigh can be expressed as the product of the location of the center of mass and the weigh vector in the body frame

$$\mathbf{M}_g = \boldsymbol{\rho}_{cm} \times \boldsymbol{R}_{IB}\mathbf{F}_{g_I} \tag{2.40}$$

where $\mathbf{F}_{g_I}$ is the weight of the airship expressed in the inertial frame.

Now that the forces and moments acting on the airship from aerodynamic, propulsive, buoyancy, and gravity have been clearly defined, the equations of motion of the airship can be put into a final form that is more comprehensive and aids in the analysis and simulation of the airship.

2.7 Equations Final Form

The dynamics and kinematics equations derived in the sections above can be put into a more comprehensive form that aids in the analysis and simulation of the airship motion later on. Equations 2.20 and 2.30 can be rearranged as follows, with the substitution of the values of the forces and moments in section 2.6

$$\begin{aligned}\dot{\mathbf{V}} = (M\boldsymbol{I}_{\mathbf{3\times 3}})^{-1}(\mathbf{F}_0 + \boldsymbol{F}_{\mathbf{1}}\dot{\mathbf{V}} + \boldsymbol{F}_{\mathbf{2}}\dot{\boldsymbol{\omega}}_{BA} + \mathbf{T}_m + \mathbf{T}_t + \mathbf{F}_{bg_B})... \\ + [\boldsymbol{\omega}_{\boldsymbol{BI}}]_\times \mathbf{V} - \boldsymbol{R}_{IB}\dot{\mathbf{W}} - [\boldsymbol{\rho}_{\boldsymbol{cm}}]_\times \dot{\boldsymbol{\omega}}_{BI} - [\boldsymbol{\omega}_{\boldsymbol{BI}}]^2_\times \boldsymbol{\rho}_{cm}\end{aligned} \tag{2.41}$$

$$\begin{aligned}\dot{\boldsymbol{\omega}}_{BI} = \boldsymbol{I}_M^{-1}(\mathbf{M}_0 + \boldsymbol{M}_{\mathbf{1}}\dot{\boldsymbol{\omega}}_{BA} + \boldsymbol{M}_{\mathbf{2}}\dot{\mathbf{V}} + \mathbf{M}_p + \mathbf{M}_{bouy} + \mathbf{M}_g... \\ + M[\boldsymbol{\rho}_{\boldsymbol{cm}}]_\times(-[\boldsymbol{\omega}_{\boldsymbol{BI}}]_\times \mathbf{V} + \dot{\mathbf{V}} + \boldsymbol{R}_{IB}\dot{\mathbf{W}}) + [\boldsymbol{\omega}_{\boldsymbol{BI}}]_\times \boldsymbol{I}_M \boldsymbol{\omega}_{BI})\end{aligned} \tag{2.42}$$

Equations 2.41 and 2.42 can be concatenated with equations 2.10 and 2.21 to from the nonlinear state space form of the equation of motion for the airship as follows:

$$\boldsymbol{C_{nss}}\dot{\mathbf{x}} = \boldsymbol{A_{nss}}\mathbf{x} + \boldsymbol{G_{nss}} \tag{2.43}$$

where

$$\boldsymbol{C}_{nss} = \begin{bmatrix} \boldsymbol{I_{3\times 3}} - (M\boldsymbol{I_{3\times 3}})^{-1}\boldsymbol{F_1} & [\boldsymbol{\rho_{cm}}]_\times - (M\boldsymbol{I_{3\times 3}})^{-1}\boldsymbol{F_2} & [\mathbf{0}]_{3\times 3} & [\mathbf{0}]_{3\times 3} \\ \boldsymbol{I}_M^{-1}(-M[\boldsymbol{\rho_{cm}}]_\times - \boldsymbol{M}_2) & \boldsymbol{I_{3\times 3}} - I_M^{-1}\boldsymbol{M}_1 & [\mathbf{0}]_{3\times 3} & [\mathbf{0}]_{3\times 3} \\ [\mathbf{0}]_{3\times 3} & [\mathbf{0}]_{3\times 3} & \boldsymbol{I_{3\times 3}} & [\mathbf{0}]_{3\times 3} \\ [\mathbf{0}]_{3\times 3} & [\mathbf{0}]_{3\times 3} & [\mathbf{0}]_{3\times 3} & \boldsymbol{I_{3\times 3}} \end{bmatrix} \tag{2.44}$$

$$\boldsymbol{A}_{nss} = \begin{bmatrix} [\boldsymbol{\omega_{BI}}]_\times & [\mathbf{0}]_{3\times 3} & [\mathbf{0}]_{3\times 3} & [\mathbf{0}]_{3\times 3} \\ -M\boldsymbol{I}_M^{-1}[\boldsymbol{\rho_{cm}}]_\times[\boldsymbol{\omega_{BI}}]_\times & \boldsymbol{I}_M^{-1}[\boldsymbol{\omega_{BI}}]_\times\boldsymbol{I}_M & [\mathbf{0}]_{3\times 3} & [\mathbf{0}]_{3\times 3} \\ \boldsymbol{R}_{IB}^T & [\mathbf{0}]_{3\times 3} & [\mathbf{0}]_{3\times 3} & [\mathbf{0}]_{3\times 3} \\ [\mathbf{0}]_{3\times 3} & \boldsymbol{\Gamma(\Omega)} & [\mathbf{0}]_{3\times 3} & [\mathbf{0}]_{3\times 3} \end{bmatrix} \tag{2.45}$$

$$\boldsymbol{G}_{nss} = \begin{bmatrix} (M\boldsymbol{I_{3\times 3}})^{-1}(\mathbf{F}_0 + \mathbf{T}_m + \mathbf{T}_t + \mathbf{F}_{bg_B}) - \boldsymbol{R}_{IB}\dot{\mathbf{W}} - [\boldsymbol{\omega_{BI}}]_\times^2\boldsymbol{\rho}_{cm}) \\ \boldsymbol{I}_M^{-1}(\mathbf{M}_0 + \mathbf{M}_p + \mathbf{M}_{bouy} + \mathbf{M}_g) + M\boldsymbol{I}_M^{-1}[\boldsymbol{\rho_{cm}}]_\times\boldsymbol{R}_{IB}\dot{\mathbf{W}} \\ \mathbf{W} \\ [\mathbf{0}]_{1\times 1} \end{bmatrix} \tag{2.46}$$

$$\begin{aligned} \mathbf{x} &= \begin{bmatrix} \mathbf{V} & \boldsymbol{\omega}_{BI} & \mathbf{r}_a & \boldsymbol{\Omega} \end{bmatrix}^T \\ &= [u \;\; v \;\; w \;\; p \;\; q \;\; r \;\; x \;\; y \;\; z \;\; \phi \;\; \theta \;\; \psi]^T \end{aligned} \tag{2.47}$$

2.8 Wind Model

The wind field experienced by the airship is simulated using an exponentially correlated stochastic model [24], termed the Exponentially Correlated Wind Model

or ECWM. The equations that govern the change of wind speed, in the inertial frame, with time are as follows

$$\begin{aligned}\dot{W}_x &= -b_w W_x + \sqrt{a_w b_w}\eta_x \\ \dot{W}_y &= -b_w W_y + \sqrt{a_w b_w}\eta_y \\ \dot{W}_z &= 0\end{aligned} \tag{2.48}$$

with a_w as a coefficient showing the extent of the mean square value of the wind, b_w the inverse time constant to show the extent of the correlation of the wind, η_x and η_y being the zero-mean Gaussian white noise. a_w and b_w are calculated as

$$a_w = 2(E\{W\}^2 + \sigma^2{}_w) \tag{2.49}$$

$$b_w = \frac{1}{\tau_w} \tag{2.50}$$

The wind is assumed to have a Gaussian distribution with zero-mean, with a standard deviation of 0.5 m/s.

The Dryden model is utilized to add turbulence effect to the wind model, this is expressed in the following differential equations that govern the states of the Dryden model

$$\begin{aligned}\dot{x}_{w1} &= -\frac{V}{L_u}x_{w1} + \sigma_u\sqrt{\frac{2V}{\pi L_u}}\eta_1 \\ \dot{x}_{w2} &= x_{w3} \\ \dot{x}_{w3} &= -\frac{V}{L_v}x_{w2} - 2\frac{V}{L_v}x_{w3} + \eta_2 \\ \dot{x}_{w4} &= x_{w5} \\ \dot{x}_{w5} &= -\frac{V}{L_w}x_{w4} - 2\frac{V}{L_w}x_{w5} + \eta_3\end{aligned} \tag{2.51}$$

where $x_{w1}, x_{w2}, x_{w3}, x_{w4}$, and x_{w5} are the states of the Dryden model, V is the airship speed, and η_1, η_2 and η_3 are zero-mean Gaussian white noise. Below is the expression of the turbulence in the inertial frame

$$\mathbf{W}_{turb} = \boldsymbol{R}_{IB}^T \boldsymbol{R}_{turb}\mathbf{x}_w \tag{2.52}$$

with $\boldsymbol{R}_{IB}$ as the rotation matrix defined earlier, and

$$\boldsymbol{R}_{turb} = \begin{bmatrix} 1 & 0 & 0 & 0 & 0 \\ 0 & \frac{\sigma_v}{\sqrt{(\pi)}} \frac{V}{L_w}^{1.5} & \sigma_v \sqrt{\frac{3V}{\pi L_v}} & 0 & 0 \\ 0 & 0 & 0 & \frac{\sigma_w}{\sqrt{(\pi)}} \frac{V}{L_w}^{1.5} & \sigma_w \sqrt{\frac{3V}{\pi L_w}} \end{bmatrix} \tag{2.53}$$

$$\mathbf{x}_w = [x_{w1} \;\; x_{w2} \;\; x_{w3} \;\; x_{w4} \;\; x_{w5}]^T \tag{2.54}$$

The equations derived in this chapter will aid in generating a high fidelity nonlinear simulation for airship flight in a wind field. They will also be used to design an Linear-Quadratic (LQ) controllers to navigate the airship through a series of waypoints as will be discussed in chapters to come.

CHAPTER 3

CONTROL AND NAVIGATION

3.1 Introduction

The ability to stabilize and control an airship is vital in any application, and due to their high sensitivity to wind and other disturbances precise control is required. The following contains a review of some of the control methods applied to airships over the past decade.

PID is a well established method of control in various applications, the AURORA airship project, which is focused on the development of sensing, control and navigation technologies for autonomous or semi-autonomous airships [25], incorporates a PID controller for the longitudinal velocity, a PD altitude controller and a PD controller for heading control are designed. A different approach incorporates a PID controller, with gains designed using H_2/H_∞ methods [26], is developed to control airship heading. The guidance and control strategy, based on a path tracking error generation methodology that takes into account the distance and angular errors of the airship with respect to a desired trajectory

Neural network augmented model inversion control is also applied to airship control [27]. The model inversion control system is a combination of feedback linearization and linear control. The theoretical aspect of applying the neural network is to compensate for the feedback linearization and modeling error. A feedback control law for way-point to way-point inertial navigation is designed for a control system featuring closed-loop guidance laws that provide autonomous navigation capability to an airship [28]. Closed loop commands keep the airship at desired speed, altitude and in-

ertial position. A dynamic inversion path-tracking control law, forcing the closed-loop system outputs to be independently controlled to follow a position command trajectory, is designed for an airship [29]. The control law shows fast correction of trajectory errors. Lyapunov stability based designs of state-feedback control laws [30] have also been implemented to the airship control problem. A backstepping methodology is utilized to design a closed-loop trajectory-tracking controller for an under actuated airship [31]. The authors state that backstepping is suitable for the cascaded nature of the vehicle dynamics and that it offers design flexibility and robustness against parametric uncertainties which are often encountered in aerodynamic modeling and air stream disturbances. Other methods including sliding mode control [32] and fuzzy logic design are implemented for airship control [33].

In this thesis the Linear-Quadratic-Regulator problem, or LQR problem is solved to acquire the optimal gains needed to design a controller for the airship. With a full-state-feedback controller design, this controller is expected to fly the airship through a series of waypoints based on commands generated by a path specific navigation algorithm. The selection of an LQR-based controller design is accredited to its ability to deal with multi variable systems in a relatively simple way, and its ease of implementation [34]. A second controller is then designed, having a Linear-Quadratic-integral (LQI) control structure; it is capable of receiving commands from a proportional navigation law and fly the airship from one waypoint to the other.

The work presented in [35] and [36] shows an LQR implantation to the airship system; in [35] however the exact gain scheduling law is not shown, neither is the navigation law used to guide the airship through flight. In [36] the gain scheduling law is implemented with 11 trim points, and the guidance law generates a commanded yaw rate based on the airship heading and the commanded heading towards the next waypoint. In this thesis however a more simplistic gain scheduling law, capable of con-

trolling the airship in straight and level flight as well as level turn flight, is introduced. Two guidance schemes are presented here; the first, a path specific guidance scheme, commands the airship to go to the next waypoint on a specific path. The other, a proportional navigation guidance scheme, commands it to go to the next waypoint by rotating its velocity vector. Both [35] and [36] assume that the states and state derivatives required to implement the control and navigation laws are available. This is not always true in reality, where some states may not be available by measurement. This issue is dressed in chapter 4 by designing and implementing a Kalman filter to estimate the required states for control, based on a minimum number of sensors.

This chapter discusses the trim conditions required for the linearization of the airship model, the linearization of the nonlinear dynamic model presented in the previous chapter, the solution to the LQR problem, the control laws and gain scheduling law used to control the airship flight, along with a guidance algorithms.

3.2 Trim conditions

The airship motion is assumed to be confined to a plane at a specific altitude, i.e. the airship will visit planar waypoints. It is also assumed that the airship speed is held constant during flight. The airship will visit all waypoints preprogrammed into the guidance algorithm in the order they are given. The AS500 airship is capable of speeds up to 12.5 m/s [7], therefore it is assumed that it can operate safely at a trim speed of 7 m/s. A trim altitude of 1000 m can be achieved if the correct mass of Helium is loaded into the hull of the AS500. Since the volume of the AS500 is 15 m^3 [7], it is assumed that the Helium in the hull will expand to that volume at the trim altitude, but no more to prevent any damage. To do so the mass of Helium loaded into the airship at sea level must account for such expansion, the following

calculations show how this is possible. The volume of the airship at sea-level and the volume at 1000 m are related as follows [4]

$$V_0 = \sigma V_{1000} \tag{3.1}$$

where σ is the ratio of air density at 1000 m and the air density at sea-level and is approximately 0.9. Setting V_{1000} equal to 15 m^3 gives $V_0 = 13.5m^3$. The volume at sea-level is related to the mass of Helium by

$$V_0 = M_{He}/\rho_{H0} \tag{3.2}$$

where M_{He} and ρ_{H_0} are the mass of Helium and the density of Helium at sea-level respectively. This calculation results in a required mass of 2.4 Kg of Helium to be loaded into the airships hull.

Now that the trim speed and altitude have been selected the phases of flight have to be identified. Since the airship will be traveling in a plane and visiting a set of waypoints it will only be required to fly straight and level and execute a level turn. This implies that two trim points have to be calculated, one for straight and level flight, the other for level turn. The trim values of the airship states are given in table 3.1 below

where $T_M, \Gamma_{T_M}, T_t, \Delta_1$, and Δ_2 are the main rotor thrust, main rotor tilt angle, the stern rotor thrust, and the deflections of the aerodynamic control surfaces.

3.3 Linear Model

To solve the LQR problem and acquire the optimal gains for controlling the airship, a linear state-space model of the airship dynamics is required. The nonlinear

Table 3.1. Trim states

State/Input	Straight and Level	Level Turn
u (m/s)	6.99	6.98
v (m/s)	0	0.194
w (m/s)	-0.365	-0.364
p (deg/s)	0	0.27
q (deg/s)	0	-0.02
r (deg/s)	0	5
z (m)	-1000	-1000
ϕ (deg)	0	-0.8
θ (deg)	-3	-3
T_M (N)	10.2	10.5
Γ_{T_M} (deg)	36.4	35.6
T_t (N)	0.2	1.7
Δ_1 (deg)	20	3.7
Δ_2 (deg)	20	20

model in equation 2.43 can be linearized about the two trim points calculated in section 3.2 and two linear state-space models having the form below are achieved

$$\delta\dot{\mathbf{x}} = \boldsymbol{A}\delta\mathbf{x} + \boldsymbol{B}\delta\mathbf{u} \tag{3.3}$$

where $\boldsymbol{A}$ is the system matrix, $\boldsymbol{B}$ is the input matrix, $\delta\mathbf{u}$ and $\delta\mathbf{x}$ are the incremental input and state vectors respectively and can be represented as follows

$$\begin{aligned} \delta\mathbf{x} &= [\delta u \;\; \delta v \;\; \delta w \;\; \delta p \;\; \delta q \;\; \delta r \;\; \delta x \;\; \delta y \;\; \delta z \;\; \delta\phi \;\; \delta\theta \;\; \delta\psi]^T \\ \delta\mathbf{u} &= [\delta T_M \;\; \delta\Gamma_{T_M} \;\; \delta T_t \;\; \delta\Delta_1 \;\; \delta\Delta_2]^T \end{aligned} \tag{3.4}$$

When linearizing the system at the straight and level trim point the following system and input matrices are generated.

$$\boldsymbol{A}_{SL} =$$

$$\left[\begin{array}{cccccccccccc}
-0.12506 & 0.00037693 & -0.16262 & 0 & 0.83481 & 0.017203 & 0 & 0 & 0 & 0 & 0.097093 & 0 \\
0.0041157 & -11.38 & -0.22913 & -44.452 & 0.0018451 & 0.86643 & 0 & 0 & 0 & -10.345 & 0.00089617 & 0 \\
-0.038647 & 0.0034293 & -2.1081 & -0.0092395 & 1.1047 & 0.00058771 & 0 & 0 & 0 & 0 & 0.90358 & 0 \\
0.0028364 & -8.9358 & -0.17682 & -49.747 & 0.002237 & 1.6226 & 0 & 0 & 0 & -11.586 & 0.0010036 & 0 \\
0.015331 & -0.00078239 & 0.42753 & 0 & -0.41083 & -0.00016844 & 0 & 0 & 0 & 0 & -0.25897 & 0 \\
0.001161 & -2.4804 & -0.054159 & -9.3868 & 0.00037975 & -0.050413 & 0 & 0 & 0 & -2.1936 & 0.00019002 & 0 \\
0.99863 & 0.0012949 & -0.052219 & 0 & 0 & 0 & 0 & 0 & 0 & 0 & 0.000965 & 0 \\
-0.0012068 & 1 & 0.0017198 & 0 & 0 & 0 & 0 & 0 & 0 & 0.36455 & 0 & 7 \\
0.052222 & -0.0016544 & 0.99863 & 0 & 0 & 0 & 0 & 0 & 0 & 0.0084492 & -7 & 0 \\
0 & 0 & 0 & 1 & 0 & -0.052293 & 0 & 0 & 0 & 0 & 0 & 0 \\
0 & 0 & 0 & 0 & 1 & 0.0016567 & 0 & 0 & 0 & 0 & 0 & 0 \\
0 & 0 & 0 & 0 & -0.001659 & 1.0014 & 0 & 0 & 0 & 0 & 0 & 0
\end{array}\right]$$

$$\boldsymbol{B}_{SL} = \left[\begin{array}{ccccc}
0.040355 & -0.2955 & 0 & 0.01631 & -0.016312 \\
0 & 0 & -0.11206 & -5.0029 & 5.0029 \\
-0.019751 & -0.1186 & 0 & 0.0014896 & -0.0014898 \\
0 & 0 & -0.10755 & -3.793 & 3.793 \\
0.0010567 & -0.029937 & 0 & -0.00042693 & 0.00042698 \\
0 & 0 & -0.032625 & -1.133 & 1.133 \\
0 & 0 & 0 & 0 & 0 \\
0 & 0 & 0 & 0 & 0 \\
0 & 0 & 0 & 0 & 0 \\
0 & 0 & 0 & 0 & 0 \\
0 & 0 & 0 & 0 & 0 \\
0 & 0 & 0 & 0 & 0
\end{array}\right]$$

When linearizing the system at the level turn trim point the following system and input matrices are generated.

$$\boldsymbol{A}_{LT} =$$

$$\left[\begin{array}{cccccccccccc}
-0.13169 & 0.17887 & -0.17658 & -0.069235 & 0.86457 & -0.78423 & 0 & 0 & 0 & 0 & 0.097086 & 0 \\
0.2968 & -11.298 & -0.1946 & -44.439 & -0.22906 & 0.8718 & 0 & 0 & 0 & -10.344 & 0.0078344 & 0 \\
-0.037486 & 0.068577 & -2.1167 & -0.18058 & 1.105 & -0.14189 & 0 & 0 & 0 & 0 & 0.90352 & 0 \\
0.21649 & -8.8707 & -0.16931 & -49.724 & -0.17571 & 1.6272 & 0 & 0 & 0 & -11.584 & 0.0087738 & 0 \\
0.015184 & -0.017082 & 0.42961 & 0.081442 & -0.411 & 0.045405 & 0 & 0 & 0 & 0 & -0.25896 & 0 \\
0.067414 & -2.4599 & -0.048073 & -9.3812 & -0.053664 & -0.049158 & 0 & 0 & 0 & -2.1932 & 0.0016611 & 0 \\
0.99857 & 0.00075631 & -0.053528 & 0 & 0 & 0 & 0 & 0 & 0 & -0.010615 & -0.00013499 & -0.19832 \\
0 & 0.9999 & 0.014128 & 0 & 0 & 0 & 0 & 0 & 0 & 0.37468 & 0 & 6.9972 \\
0.053533 & -0.014108 & 0.99847 & 0 & 0 & 0 & 0 & 0 & 0 & 0.19801 & -6.9972 & 0 \\
0 & 0 & 0 & 1 & 0.0007574 & -0.053605 & 0 & 0 & 0 & 0 & 0.087392 & 0 \\
0 & 0 & 0 & 0 & 0.9999 & 0.014128 & 0 & 0 & 0 & -0.087141 & 0 & 0 \\
0 & 0 & 0 & 0 & -0.014148 & 1.0013 & 0 & 0 & 0 & 0 & -0.0046779 & 0
\end{array}\right]$$

$$\boldsymbol{B}_{LT} = \begin{bmatrix} 0.040956 & -0.30753 & 0 & 0.072467 & -0.072468 \\ 0 & 0 & -0.11206 & -5.0065 & 5.0065 \\ -0.019501 & -0.13176 & 0 & 0.0066183 & -0.0066184 \\ 0 & 0 & -0.10755 & -3.7955 & 3.7955 \\ 0.0011184 & -0.031858 & 0 & -0.0018969 & 0.0018969 \\ 0 & 0 & -0.032625 & -1.1337 & 1.1337 \\ 0 & 0 & 0 & 0 & 0 \\ 0 & 0 & 0 & 0 & 0 \\ 0 & 0 & 0 & 0 & 0 \\ 0 & 0 & 0 & 0 & 0 \\ 0 & 0 & 0 & 0 & 0 \\ 0 & 0 & 0 & 0 & 0 \end{bmatrix}$$

3.4 The LQR Problem

3.4.1 Problem statement

The Linear-Quadratic-Regulator problem is in its essence an optimization problem that deals with finding a state-feedback control law of the form $\delta\mathbf{u} = -\boldsymbol{K}\delta\mathbf{x}$ that minimizes a quadratic performance index subject to a linear dynamical constraint in equation 3.3 [34]. The performance index is of the following form:

$$J = \int_0^\infty (\delta\mathbf{x}^T \boldsymbol{Q} \delta\mathbf{x} + \delta\mathbf{u}^T \boldsymbol{R} \delta\mathbf{u}) dt \tag{3.5}$$

where $\boldsymbol{Q}$ is a diagonal $n \times n$ weighting matrix and is typically positive-semidefinite, n is the number of states which is equal to 12. $\boldsymbol{R}$ is a diagonal $m \times m$ positive-definite weighting matrix, where m is the number of inputs and is equal to 5 in the AS500 airship model.

3.4.2 Selection of Q and R matrices

Various methods of selecting the $\boldsymbol{Q}$ and $\boldsymbol{R}$ matrices are available in the literature. The elements in both $\boldsymbol{Q}$ and $\boldsymbol{R}$ are regarded as penalties of how important a state is versus the control effort [37], one method is to select $\boldsymbol{Q} = \boldsymbol{C}^T\boldsymbol{C}$ and $\boldsymbol{R} = \boldsymbol{B}\boldsymbol{B}^T$ and after the first run the values will be tuned for a required performance [38], another method is based on deriving a mathematical relation between the sys-

tem response and the $\boldsymbol{Q}$ and $\boldsymbol{R}$ weighting matrices [39], this however is only done for a two-order system. Since the goal of this thesis is not to derive the mathematical formulation for selecting a $\boldsymbol{Q}$ and $\boldsymbol{R}$ matrix for the twelfth order airship system, the method selected to acquire an initial value of diagonal weighting matrices is Bryson's law [40].

Bryson's law suggests the selection of diagonal elements for $\boldsymbol{Q}$ based on the inverse of the maximum allowable value for each state, and diagonal elements for $\boldsymbol{R}$ based on the inverse of the maximum allowable value for each input. This approach is utilized in designing the airship controller, after which the diagonal elements are tuned to render a satisfactory performance.

3.4.3 Problem solution

After the selection of the $\boldsymbol{Q}$ and $\boldsymbol{R}$ matrices the LQR problem can be solved by first solving the algebraic matrix Riccati equation of the form shown below.

$$\boldsymbol{A}^T\boldsymbol{P} + \boldsymbol{P}\boldsymbol{A} + \boldsymbol{Q} - \boldsymbol{P}\boldsymbol{B}\boldsymbol{R}^{-1}\boldsymbol{B}^T\boldsymbol{P} = 0 \tag{3.6}$$

The solution $\boldsymbol{P}$ of equation 3.6 is used to acquire the optimal gains as follows

$$\boldsymbol{K} = \boldsymbol{R}^{-1}\boldsymbol{B}^T\boldsymbol{P} \tag{3.7}$$

When solving the LQR problem for the two systems shown in section 3.3 a set of two gain matrices is achieved as follows.

$\boldsymbol{K}_{SL} =$

$$\begin{bmatrix}
-0.0040 & -0.0026 & -0.3223 & 0.0003 & -1.816 & 0.0109 & 0.0003 & 0 & 0.02819 & -0.0006 & -0.7183 & 0.0032 \\
-0.1236 & 0.0023 & -1.2294 & 0.0004 & -6.9414 & -0.0116 & 0 & 0 & 0.1114 & -0.002 & -2.5894 & -0.0014 \\
-0.0004 & 0.0202 & 0 & -0.0006 & -0.0005 & -0.0930 & 0 & 0 & 0 & 0.0016 & 0.0010 & -0.0408 \\
-0.0002 & 0.6340 & 0.0224 & 0.0421 & 0.0790 & -3.2655 & 0 & -0.0002 & -0.0003 & 0.0416 & 0.0230 & -2.2377 \\
0.0002 & -0.6340 & -0.0224 & -0.0421 & -0.0790 & 3.2655 & 0 & 0.0002 & 0.0003 & -0.0416 & -0.0230 & 2.2377
\end{bmatrix}$$

$$\boldsymbol{K}_{LT} =$$

$$\begin{bmatrix}
0.0008 & -0.0003 & -0.2693 & 0.0051 & -1.5172 & -0.0141 & 0.0003 & 0 & 0.02497 & 0.1862 & -0.6023 & 0.0377 \\
-0.1137 & 0.0126 & -1.147 & 0.0248 & -6.4934 & -0.1423 & 0 & 0 & 0.1113 & 0.7764 & -2.4273 & 0.0486 \\
-0.0008 & 0.0196 & -0.0018 & -0.0004 & -0.0138 & -0.0907 & 0 & 0 & 0.0004 & 0.0035 & -0.0094 & -0.0402 \\
-0.0161 & 0.6239 & 0.0112 & 0.0454 & -0.0587 & -3.2351 & 0 & -0.0002 & 0.0099 & 0.0585 & -0.1646 & -2.2355 \\
0.0161 & -0.6239 & -0.0113 & -0.0454 & 0.0586 & 3.2351 & 0 & 0.0002 & -0.0095 & -0.0585 & 0.1646 & 2.2355
\end{bmatrix}$$

3.4.4 Set-point tracking control law

The gains calculated from the LQR problem solution in section 3.4.3 correspond to a regulation problem. A regulation problem in control theory translates to regulating the value of all the states of the system to zero. This however is not the requirement of the designed controller. It is desired that the states of the airship be driven to the corresponding trim values of the current flight segment. This is accomplished by a set-point tracking control law, which is of the form

$$\mathbf{u} = -\boldsymbol{K}(\mathbf{x} - \mathbf{x}_{trim}) + \mathbf{u}_{trim} \tag{3.8}$$

where $\mathbf{x}$ is the state vector, $\mathbf{x}_{trim}$ is the value of the trim states at the current flight condition, $\mathbf{u}_{trim}$ are the trim values for the inputs at the same flight condition, and $\boldsymbol{K}$ is the same gain matrix calculated earlier. Figure 3.1 shows an illustrative block diagram of a set-point tracking controller.

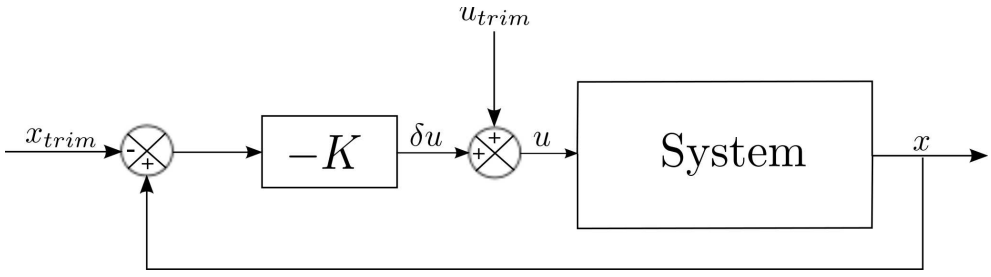

Figure 3.1. Block diagram of a set-point tracking controller.

3.5 The LQI Problem

The LQI problem is similar to the LQR one in which it is an optimization problem, when solved finds the feedback control law of the following form $\delta\mathbf{u} = -K\mathbf{z}$, where $\mathbf{z} = [z_1 \;\; z_2]$ with $z_1 = \mathbf{x} - \mathbf{x}_{trim}$ and $z_2 = \mathbf{x}_i$. $\mathbf{x}_i$ is the output of the integrator in figure 3.2. The LQI is applied to a system having an output, $\mathbf{y}$, of state rates which are compared to a reference signal $\mathbf{r}$, this generates an error. The error is then integrated, giving $\mathbf{x}_i$ to be used in the control law. The cost function for the LQI problem is of the following form

$$J = \int_0^\infty (\mathbf{z}^T \boldsymbol{Q} \mathbf{z} + \delta\mathbf{u}^T \boldsymbol{R} \delta\mathbf{u}) dt \tag{3.9}$$

The LQI problem is solved to acquire the optimal gains in order to control the

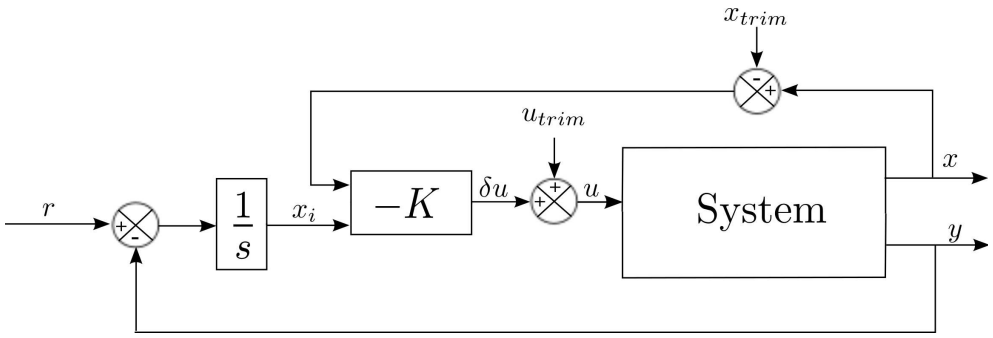

Figure 3.2. Block diagram of a set-point tracking LQI controller.

airship motion and navigate its flight through a series of waypoints. A proportional navigation law, introduced later in this chapter, will provide commanded turn rates based on the airship location relevant to the next waypoint. The commanded turn rate is compared to the airship actual turn rate in an LQI controller to generate the required commands for turning the airship towards the next waypoint.

3.6 Gain Scheduling Law

In order to have a smooth transition between the set of gain matrices that were previously generated, a gain scheduling law is designed here. When the airship is arrives at a waypoint, it must initiate a level turn. The heading command generated by the guidance algorithm discussed later. After the turn is initiated the gains of the controller have to transition from the ones corresponding to the straight and level flight condition to those corresponding to the level turn condition, this is achieved by a gain scheduling. The idea of gain scheduling spurs from the fact that a linear controller will work well as long as the system is in the neighborhood of the trim point, large deviations from the trim point may lead to unsatisfactory performance, hence the idea of gain scheduling. In gain scheduling the system is linearized at different points and gains corresponding to each linearized system are calculated. A scheduling law in effect interpolates the values of the gains based on a scheduling parameter that is a function of a scheduling variable. The proposed gain scheduling law for controlling the airship based on the LQR designed gains is

$$\boldsymbol{K} = (1 - \sigma)\boldsymbol{K}_{SL} + \sigma\boldsymbol{K}_{LT} \tag{3.10}$$

where σ is the scheduling parameter, and is a function of the turn rate $\dot{\psi}$. The selection of the turn rate as a scheduling variable is based on the fact that the airship is only required to fly straight towards the current waypoint and upon arriving executing a level turn towards then next one. This translates into σ having a value between 0 and 1, where at $\sigma = 0$ the airship is flying straight and level and at $\sigma = 1$ the airship is turning. The scheduling parameter as a function of the scheduling variable is set to be a linear function as follows

$$\sigma = a_1|\dot{\psi}| + a_2 \tag{3.11}$$

The constants a_1 and a_2 can be solved for by substituting the values of 0 and 1 for σ in equation 3.11 as follows

$$a_1\dot{\psi}_{SL} + a_2 = 0 \tag{3.12}$$

$$a_1\dot{\psi}_{LT} + a_2 = 1 \tag{3.13}$$

from equation 3.12

$$a_1 = -\frac{a_2}{\dot{\psi}_{SL}} \tag{3.14}$$

by substituting equation 3.14 into equation 3.13 we get

$$-\frac{a_2}{\dot{\psi}_{SL}}\dot{\psi}_{LT} + a_2 = \frac{\dot{\psi}_{SL} - \dot{\psi}_{LT}}{\dot{\psi}_{SL}}a_2 = 1 \tag{3.15}$$

therefore

$$a_2 = \frac{\dot{\psi}_{SL}}{\dot{\psi}_{SL} - \dot{\psi}_{LT}} \tag{3.16}$$

substituting equation 3.16 into equation 3.14 yields

$$a_1 = -\frac{1}{\dot{\psi}_{SL} - \dot{\psi}_{LT}} \tag{3.17}$$

and by further substituting equations 3.16 and 3.17 into 3.11 the scheduling parameter expression is

$$\sigma = -\frac{1}{\dot{\psi}_{SL} - \dot{\psi}_{LT}}\dot{\psi} + \frac{\dot{\psi}_{SL}}{\dot{\psi}_{SL} - \dot{\psi}_{LT}} \tag{3.18}$$

Since for a straight and level flight the turn rate is required to be zero, equation 3.18 simplifies to

$$\sigma = \frac{|\dot{\psi}|}{\dot{\psi}_{LT}} \tag{3.19}$$

A saturation limit is imposed on equation 3.19, where when the value of $|\dot{\psi}|$ is larger than $\dot{\psi}_{LT}$, the value of σ is one, this is mathematically formulated as follows

$$\sigma = sat\left(\frac{|\dot{\psi}|}{\dot{\psi}_{LT}}\right) \ : \ \sigma = 1, \ \ \forall \ \ |\dot{\psi}| > \dot{\psi}_{LT} \tag{3.20}$$

It should be noted that the value of $|\dot{\psi}|$ in equation 3.20 while flying in straight and level should, theoretically, be zero. However, due to sensor imperfections while measuring the turn rate and as a consequence of the dynamics of the closed-loop feedback system, the value of $|\dot{\psi}|$ during straight and level flight will not be perfectly zero. This causes the scheduling parameter σ to not strictly be equal to zero during straight and level flight as well. This generates an interpolated value of the gains during straight and level flight, which in turn introduces additional modeling errors. This effect will also be amplified later on when the estimated values of the states are bed back to the controller from a Kalman filter.

3.7 Guidance Algorithms

3.7.1 Track-specific guidance law (TS)

Now that a controller has been designed to control the flight of the airship, commands have to be sent to that controller in order for it to know what the airship is to do, these commands are generated by the navigation algorithm. Based in these commands the controller generates signals to the inputs of the airship to correct their values in order to achieve the required flight. A track-specific guidance law is discussed in this section.

It is required to fly the airship through a series of planar waypoints, for illustrative purposes lets name the waypoints A, B, C and D, and assume the airship will visit them in that order. The guidance law tracks the waypoints in pairs, i.e when the airship just passes waypoint A and is on its way to waypoint B, a geometric heading based in the location of this pair of waypoints is calculated from equation 3.21, where A_x, A_y, B_x, and B_y are the x and y coordinates of waypoints A and B respectively.

$$\chi_{geo} = \tan^{-1}\left(\frac{B_y - A_y}{B_x - A_x}\right) \tag{3.21}$$

The heading of the airship is calculated based in its projected ground speed as

$$\chi_a = \tan^{-1}\left(\frac{\dot{y}}{\dot{x}}\right) \tag{3.22}$$

using the geometric and airship headings a desired heading angle is calculated from the following function

$$\chi_d = \frac{\pi}{2}\tanh\left(\frac{d}{L_{des}}\right) \tag{3.23}$$

where d is the normal distance to the virtual straight line path connecting the waypoints, shown in figure 3.3, and is calculated as follows

$$d = ||\mathbf{R}_t|| \sin\left(\chi_{geo} - \chi_a\right) \tag{3.24}$$

where $||\mathbf{R}_t||$ is the distance traveled from waypoint a, and L_{des} is a design parameter which is a function of the airship speed calculated as follows

$$L_{des} = ||\mathbf{V}||\tau \tag{3.25}$$

with τ being a performance design parameter. The commanded yaw angle provided to the set-point tracking controller in equation 3.8 is calculated as follows

$$\psi_{comm} = \chi_d - \beta. \tag{3.26}$$

where β is the airship side-slip angle.

The airship is flown in a straight line at that calculated desired heading until it is within a predefined waypoint proximity zone of a specified radius. When the waypoint proximity zone is breached the navigation algorithm switches to waypoints B and C to calculate a new heading so that the airship turns and flies towards waypoint C. The guidance law methodology is illustrated in figure 3.3.

It should be noted that the guidance law in equation 3.23 is limited to the case where vectors V and R_t are as close to being parallel as possible, it would work fine for minor deviations as well.

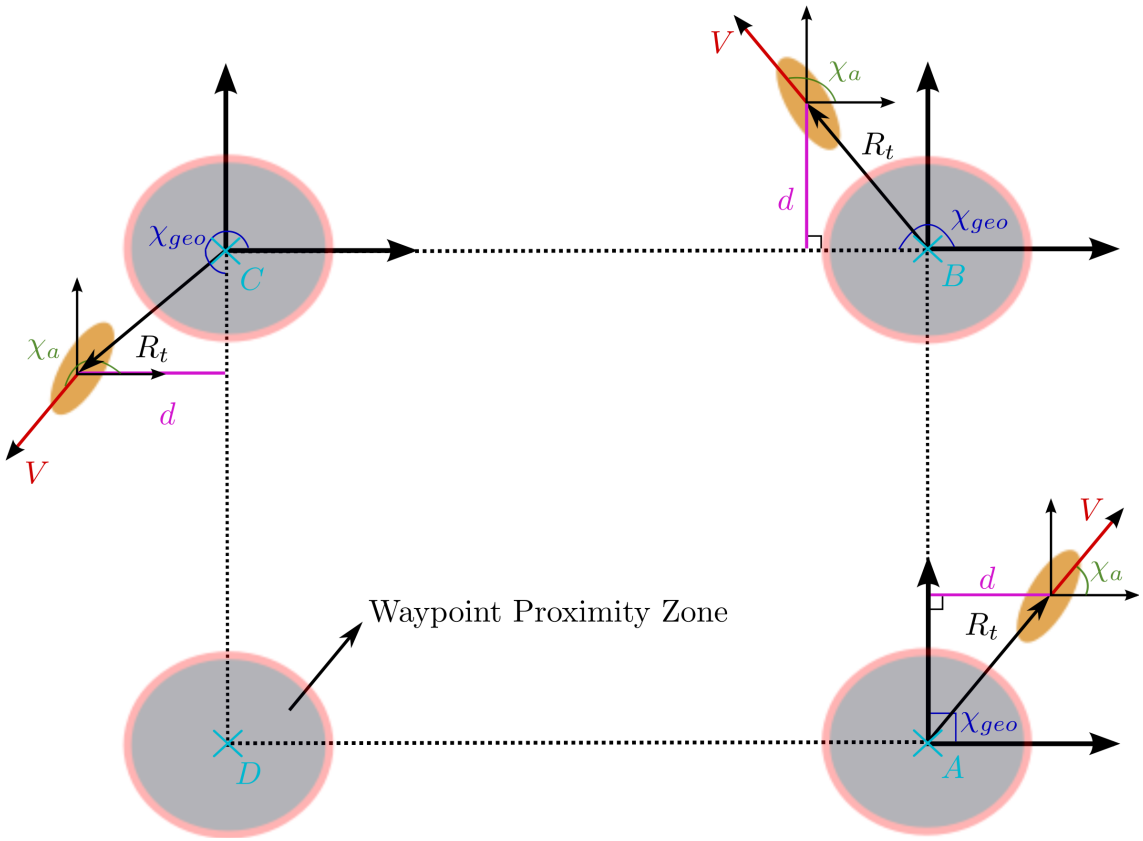

Figure 3.3. Illustration of track-specific guidance law methodology.

3.7.2 Proportional navigation guidance law

Proportional navigation (PN) is a method of guidance that has been applied to missiles for terminal guidance [41], it is probably the most popular guidance methods for short-range intercept [42], it has also bee applied to aircraft for purpose of collision avoidance [43]. In this section a proportional navigation guidance law is derived for airship waypoint navigation purposes, where the waypoint is considered a non-moving target and the airship is guided towards that target. Yaw rate commands are generated by the PN law and fed into the LQI controller, shown in figure 3.2, as reference signals $\mathbf{r}$. The reference signal is compared with the airship yaw rate and the error generates control signals to yaw the airship towards the next waypoint.

The engagement geometry for planar pursuit of a waypoint by the airship is shown in figure 3.4. Where χ_a, χ_{LOS}, $\mathbf{R}_{LOS}$, $\mathbf{V}$ and a_{PN} are the airship heading, Line-of-Sight (LOS) heading, the LOS vector, the airship velocity vector, and the commanded acceleration by the PN guidance law. The commanded acceleration is dictated by the PN law to be

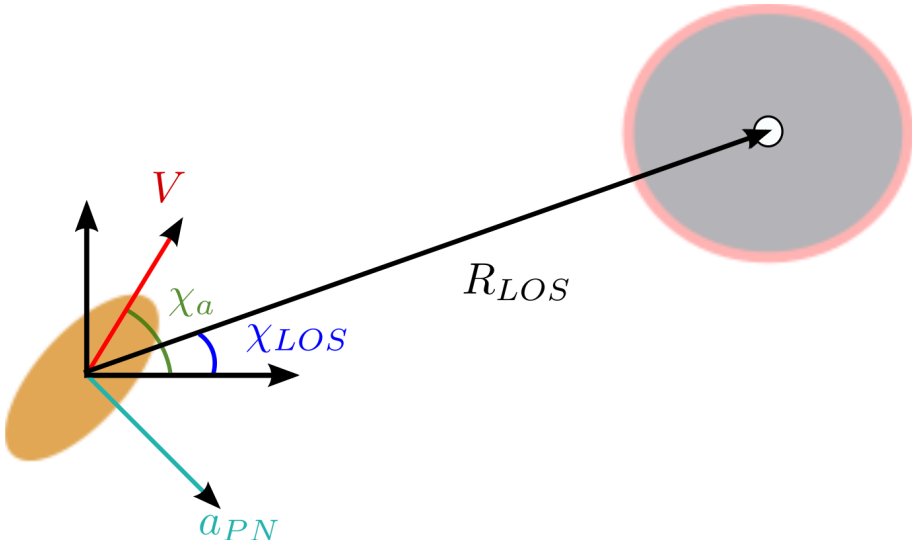

Figure 3.4. Engagement geometry for planar pursuit of a waypoint.

$$a_{PN} = N\dot{\chi}_{LOS}V_c \tag{3.27}$$

where N is the navigation constant with values usually ranging from 2 to 5, $\dot{\chi}_{LOS}$ is the rate of rotation of the LOS, and V_c is the airship closing velocity on the waypoint. From the engagement geometry in figure 3.4, it can be seen that

$$\dot{\chi}_{LOS} = \frac{-||\mathbf{V}||\sin(\chi_a - \chi_{LOS})}{||\mathbf{R}_{LOS}||} \tag{3.28}$$

$$V_c = ||\mathbf{V}||\cos(\chi_a - \chi_{LOS}) \tag{3.29}$$

The value of the commanded heading rate for the airship can be calculated from equation 3.27 to be [41]

$$\dot{\chi}_{comm} = \frac{a_{PN}}{V_c} \tag{3.30}$$

to supply the controller with a commanded yaw rate it is assumed that the commanded heading rate from the PN law is equal to a commanded yaw rate, therefore

$$\dot{\psi}_{comm} = \dot{\chi}_{comm} \tag{3.31}$$

The value of $\dot{\psi}_{comm}$ is given as a reference signal in the previously design LQI controller to force the airship to track the yaw rate commands generated by the PN-law, therefore guiding it through any series of waypoints.

3.8 Results and Discussion

3.8.1 Flight with no wind

The simulation is initialized with the airship at the origin point of the inertial frame, the airship will then travel to four preprogrammed waypoints until it has visited each one of them. The radius of the waypoint proximity zone around each waypoint is set to 40 m, the altitude is held at 1000 m, and the speed is kept constant at a value of 7 m/s. The simulation is carried out for both guidance laws without wind effects, and is terminated when the airship has visited all the waypoints within a proximity equal to the waypoint proximity zone radius. Below is a discussion of the simulation results.

The results for using the track-specific guidance law are shown in figures 3.5 to 3.10. Figure 3.5 shows the time history of the body-axis velocities from the simulation, it is notable that the forward speed is held at the value of 7 m/s, and the side-speed has three major peaks each corresponding to the turns executed by the airship. Figure 3.6 shows the angular rates of the airship, it is noticed that the yaw rate has three

distinguishable peaks of approximately 8 deg/s, also corresponding to the turns the airship executed to visit the all the waypoints. Figure 3.7 shows the pitch angle held approximately constant at the trim value, however an interesting observation can be made about the roll and yaw angles; it seems that when the airship experiences a positive yaw angle change, a negative bank angle is experienced, which is unlike the case for a conventional aircraft where the bank angle is inward towards the yaw angle. This can be explained by examining figure 3.8, where the tail thrust generated by the tail rotor acts on the airship to change the yaw angle, however due to its location being above the center of gravity the effect is translated to a negative bank angle which is considerably small (-2.5 deg). Figure 3.9 shows the time history of the airship inertial position where the maximum deviation from the trim altitude is 1 m, the speed of the airship can be seen in figure 3.10 with a maximum deviation from the trim speed of 0.5 m/s.

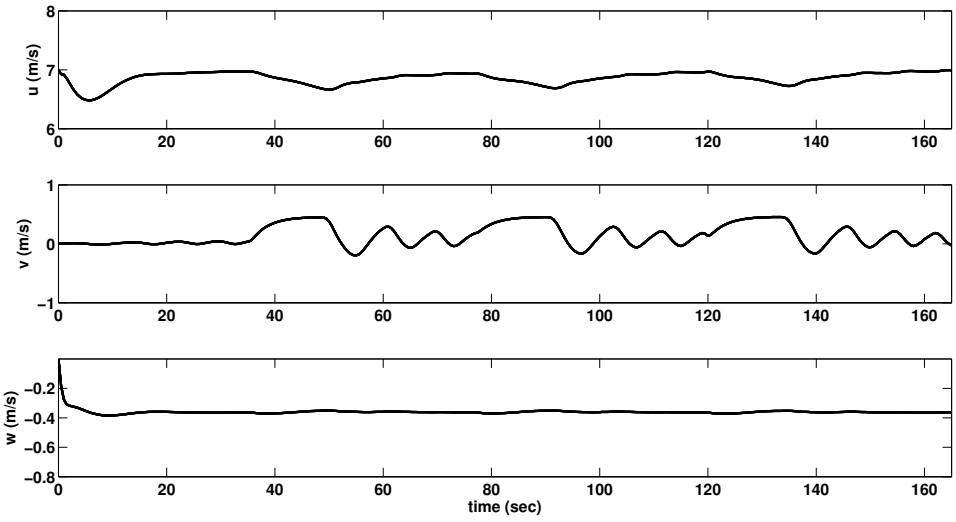

Figure 3.5. Time history of body-axis velocities for track-specific guidance in no wind condition.

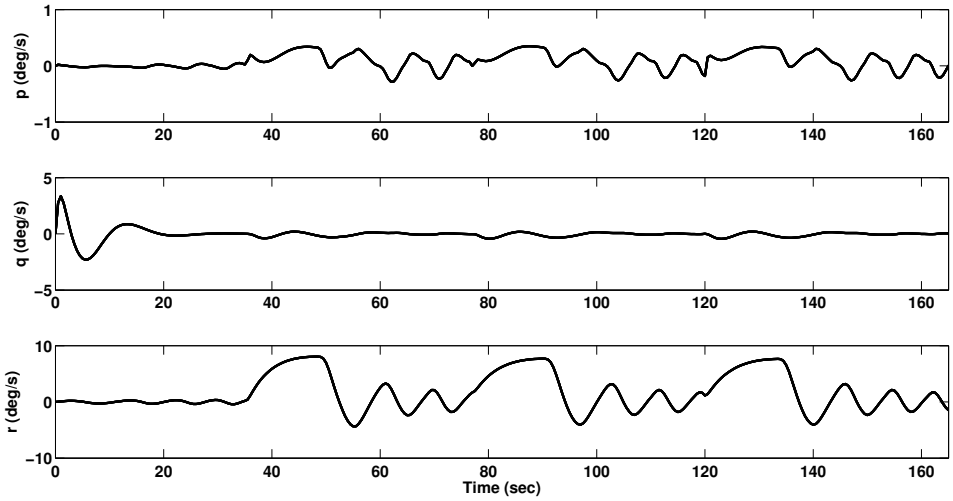

Figure 3.6. Time history of body-axis angular rates for track-specific guidance in no wind condition.

The results for employing the PN guidance law in tandem with the LQI controller are displayed in figures 3.11 to 3.16. Figure 3.11 shows that the value of the side-speed differs from that when the specific-path guidance law is implemented; there are no outstanding peaks in the values, however the behavior is that of sustaining a specific value less that 0.5 m/s after the first 40 seconds of the simulation. This indicates that the airship is in a continued turning motion. Unlike the value in figure 3.5, where three identifiable peaks suggest that the airship executes three clear turns. The same argument can be made for the yawing and rolling body rates in figure 3.12; where the values indicate a continuous yaw and roll after the first 40 seconds of the simulation i.e. after the first waypoint is reached. This result shows the nature of the PN guidance law, where an acceleration is constantly commanded to change the direction of the velocity vector towards the target, in this case the waypoint. The control inputs generated by the system are shown in figure 3.14, followed by the time

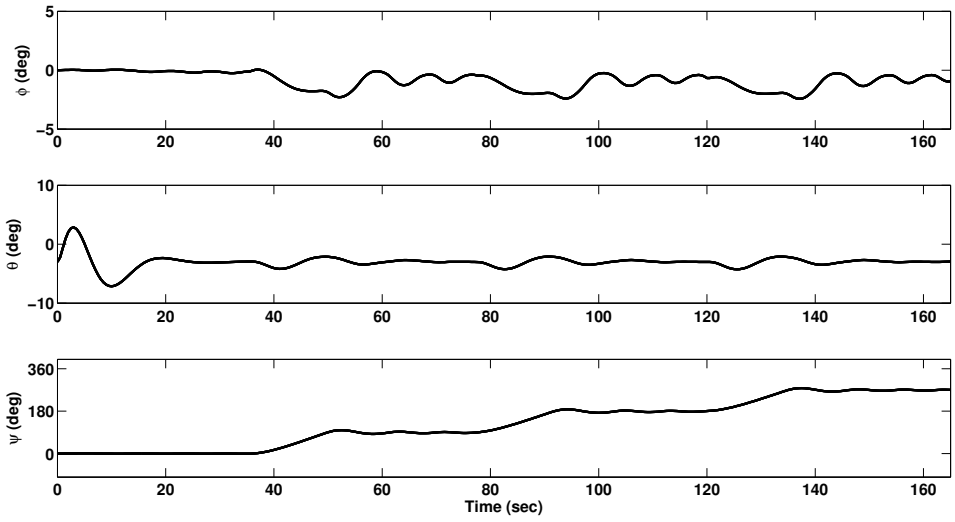

Figure 3.7. Time history of attitude angles for track-specific guidance in no wind condition.

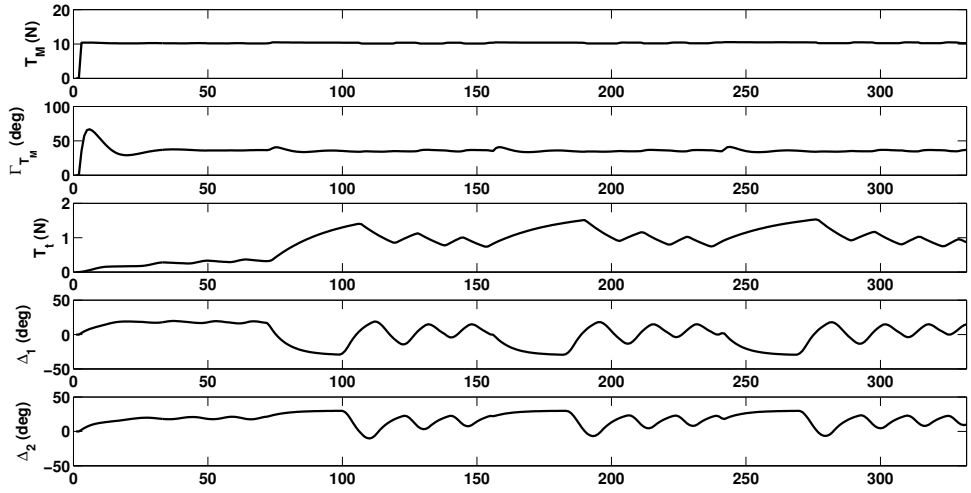

Figure 3.8. Airship control inputs for track-specific guidance in no wind condition.

history of the inertial position of the airship in figure 3.15 which displays the con-

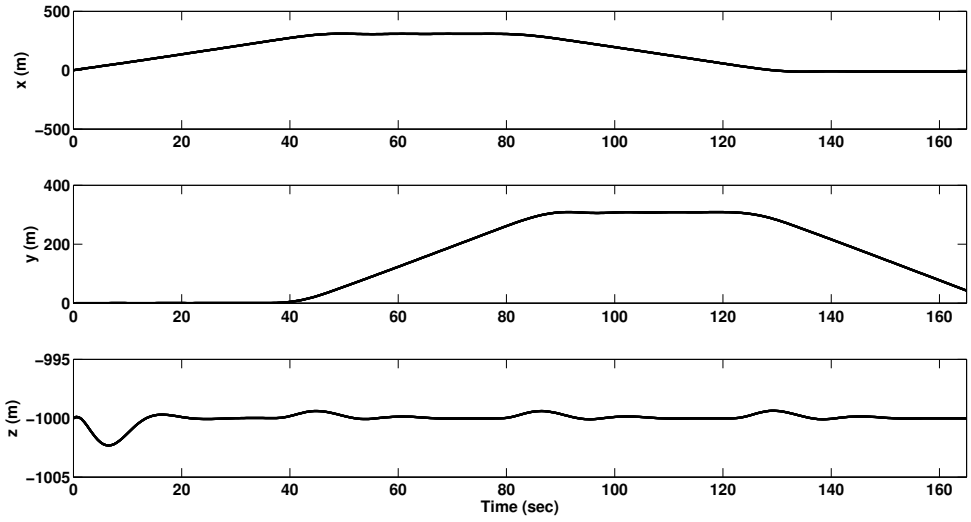

Figure 3.9. Time history of inertial positions for track-specific guidance in no wind condition.

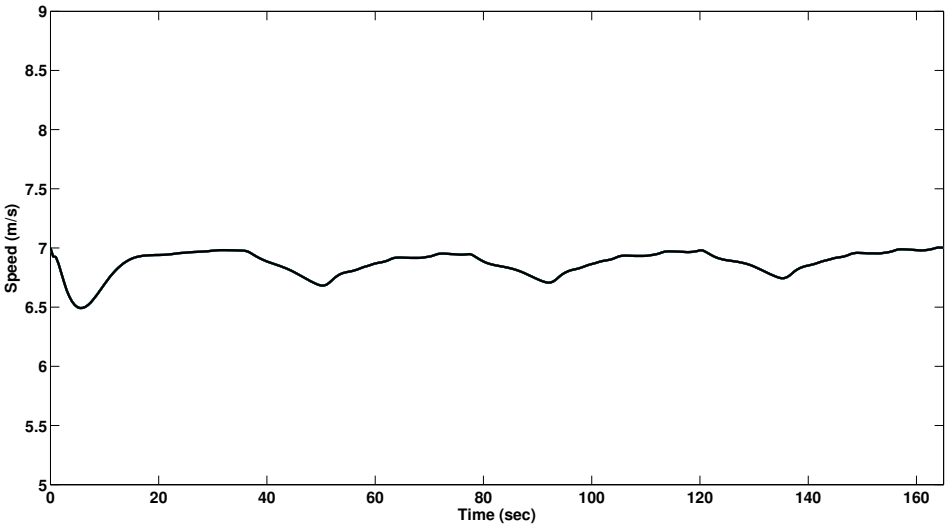

Figure 3.10. Time history of airship speed for track-specific guidance in no wind condition.

trollers ability to efficiently hold the altitude. The speed is also shown to be kept constant at 7 m/s, as shown in figure 3.16.

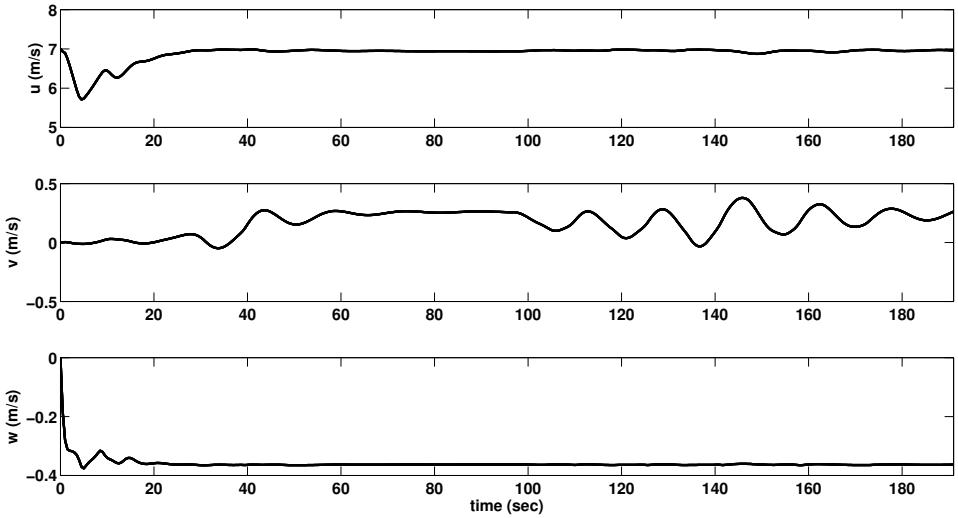

Figure 3.11. Time history of body-axis velocities for proportional navigation guidance in no wind condition.

The flight trajectory is shown in figure 3.17. The fundamental difference between the two guidance laws can be clearly seen in this figure; the track-specific guidance law attempts to track a reference trajectory, therefore flying straight in between waypoints and turning in the vicinity of them to navigate towards the next one. The PN law however puts the airship on a continuous arc-like trajectory after it has passed the first waypoint, this is caused by continously generating acceleration commands to change the heading if the airship towards the next waypoint. Both guidance laws are capable of flying the airship through the waypoints, each however in its own way, therefore they are both accepted candidates for the purpose of visiting each waypoint. It can be seen from figure 3.17 that for the case of the TS guidance

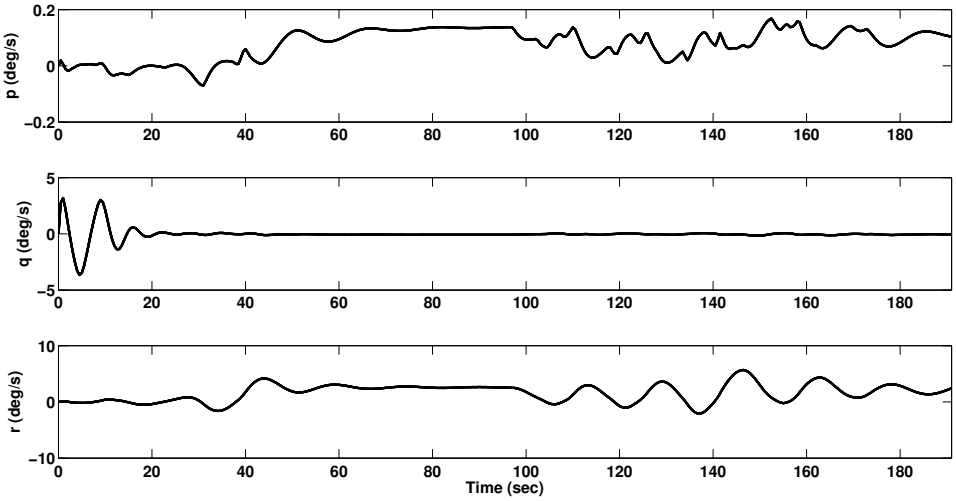

Figure 3.12. Time history of body-axis angular rates for proportional navigation guidance in no wind condition.

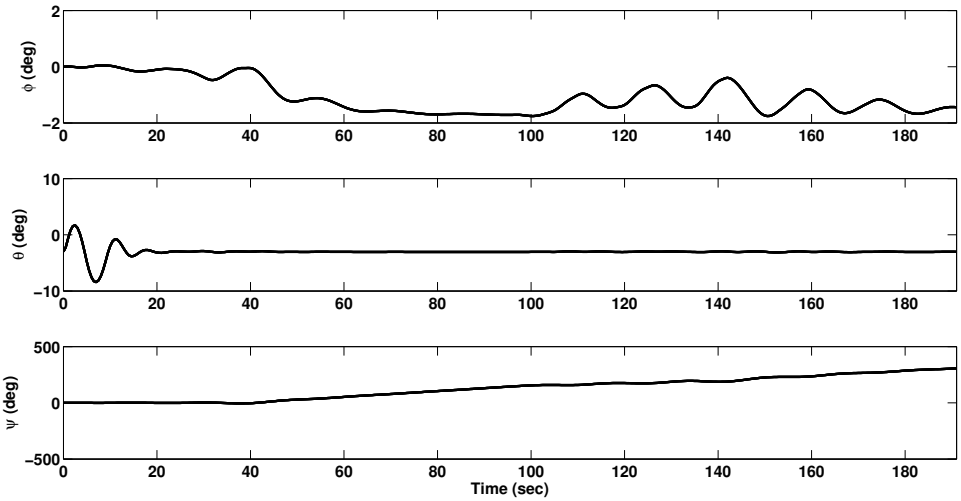

Figure 3.13. Time history of attitude angles for proportional navigation guidance in no wind condition.

law, there exist a steady-state error in each segment. The maximum deviation from the reference trajectory is 12.4 m in the last (fourth) segment. This is attributed to

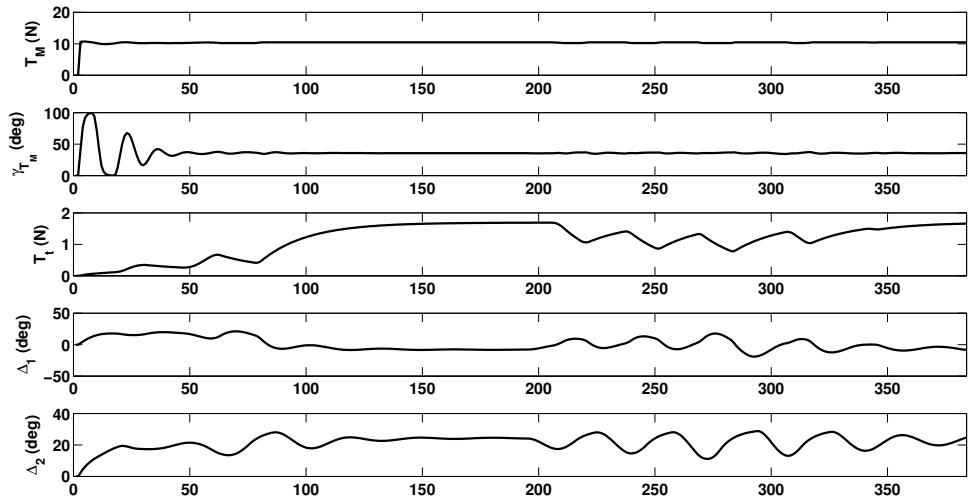

Figure 3.14. Airship control inputs for proportional navigation guidance in no wind condition.

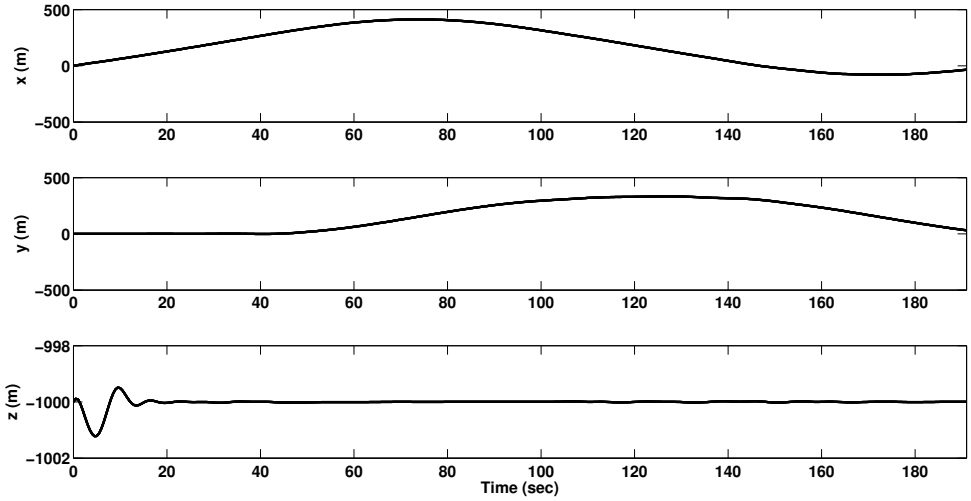

Figure 3.15. Time history of inertial positions for proportional navigation guidance in no wind condition.

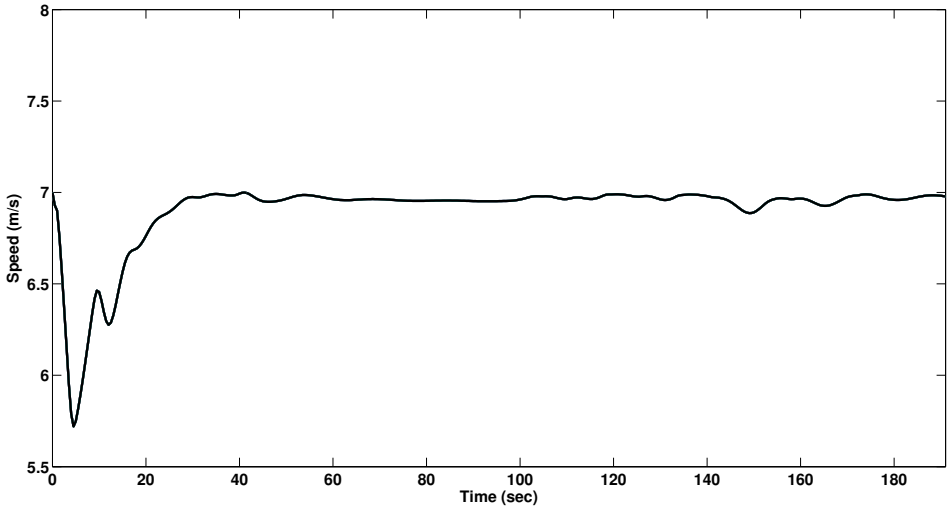

Figure 3.16. Time history of airship speed for proportional navigation guidance in no wind condition.

the fact mentioned earlier in section 3.6; after executing a turn the value of the turn rate, that is used to calculated the scheduling parameter σ from equation 3.20, is not strictly zero. This causes the value if σ to not be strictly zero which in turn causes the steady-state error. This is further demonstrated in subsection 3.8.4 ahead.

3.8.2 Flight in the presence of wind

The same simulation is now run with two differences; the first being that the airship experiences a North-East wind field generated using the wind model in section 2.8 and shown in figure 3.18, and the second being the change of the waypoint proximity zone radius to 60 m to accomedate the track-specific guidance law's inability to visit all the waypoints if the raduis is kept at 40 m in the presence of wind. The raduis is also changed to 60 m for the PN guidance law for the sake of consistency. As a result of the wind presence the airship flight path, for the track-specific guidance law, can be seen to be shifted when compared to the no-wind flight path as shown in figure

3.19, the wind field direction is indicated in the figure. The maximum deviation from the reference trajectory for the TS guidance law in the presence of wind is 30.6 m, and it occurs in the second segment. This shows how much the airship dynamics are effected by the wind, and that this is an issue worthy of solving in order to to enhance the performance of the controller. This is done by designing a Kalman filter algorithm that estimates the wind speeds and feeds it back to the navigation algorithm so that it can generate signals, with knowledge of the wind, to the controller in order to get better performance during flight. This will be discussed in the next chapter. For the PN guidance law, the trajectory is also shifted as can be seen in figure 3.20. However since that the purpose of the PN law is to reach each waypoint traveling on any trajectory possible, the wind effect is not too severe it terms of performance for the airship manages to visit each waypoint.

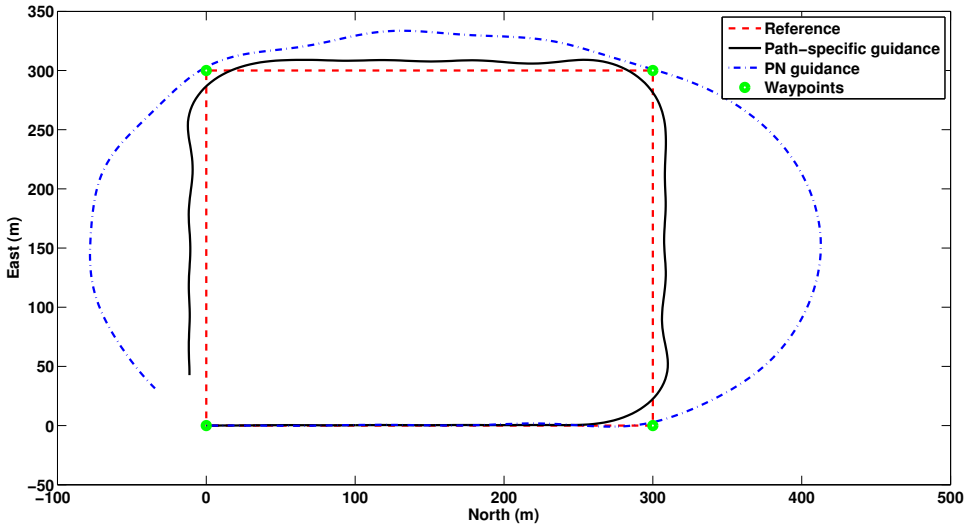

Figure 3.17. Airship flight trajectory in no wind condition.

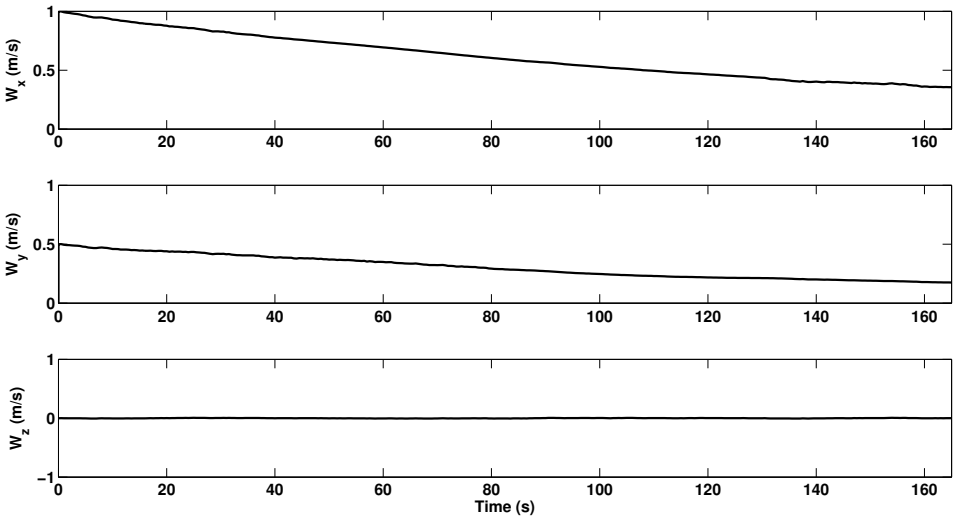

Figure 3.18. Wind field the airship experiences.

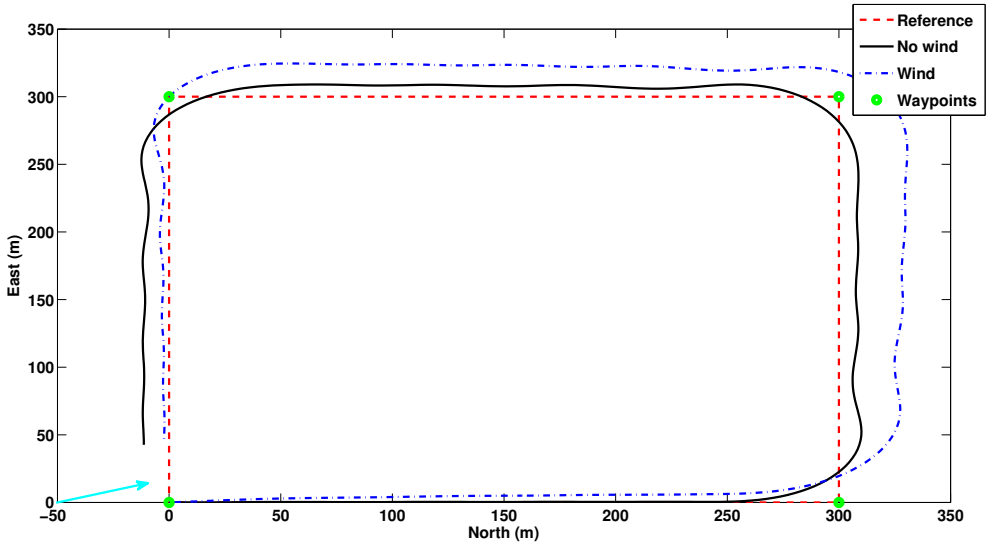

Figure 3.19. Flight trajectories with and without the influence of North-East wind for path specific guidance.

3.8.3 Waypoint proximity zone radius sensitivity

With any system the response is a product of the requirements. One of the requirements in navigating the airship through a series of waypoints is the waypoint

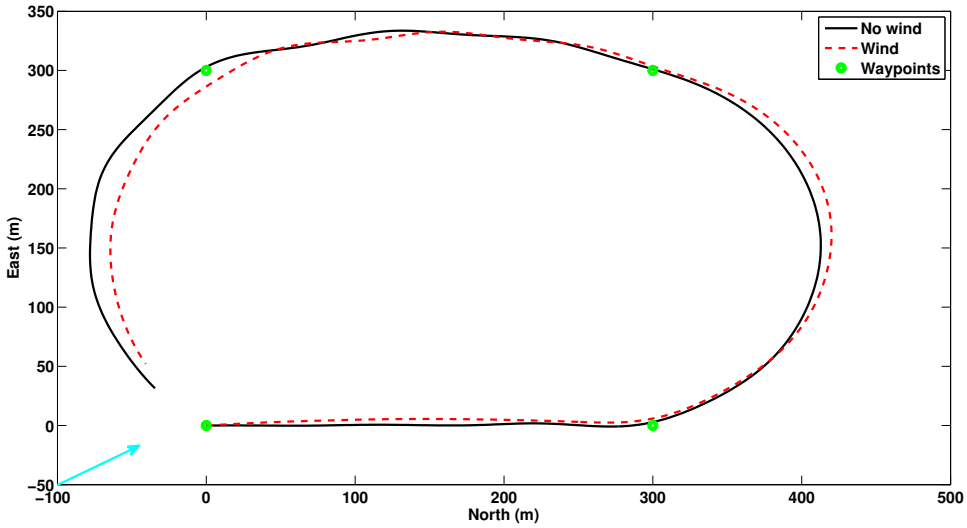

Figure 3.20. Flight trajectories with and without the influence of North-East wind for proportional navigation guidance.

proximity zone radius. Both the track-specific and PN guidance laws behave differently for different values of the waypoint proximity radius, in this subsection the sensitivity of both guidance laws to the waypoint proximity radius is investigated. Simulations for both guidance laws are conducted in the presence of the wind field in figure 3.18. It is observed that the track-specific guidance law can not meet the requirement of visiting every waypoint with a waypoint proximity radius less than 50 m. The PN guidance law however is capable of meeting a 5 m waypoint proximity radius. This is due to the fact that the track-specific guidance law has an extra constraint of minimizing the perpendicular distance to a straight line path between each waypoint set. The PN guidance law however is only concerned with arriving at the target, which is the next waypoint, the path it travels between waypoints is only dictated by the lateral accelerations commanded by the PN law.

The result for simulating the sensitivity of the track-specific guidance law to the waypoint proximity zone radius is shown in figure 3.21. It can bee seen that the for the smallest radius (50 m) the deviation form the reference trajectory is largest, then decreases as the value of the waypoint proximity radius increases up until the value of 70 m. That point shows to have the least deviation, but as the radius is increases past 70 m the deviation starts to increase again.

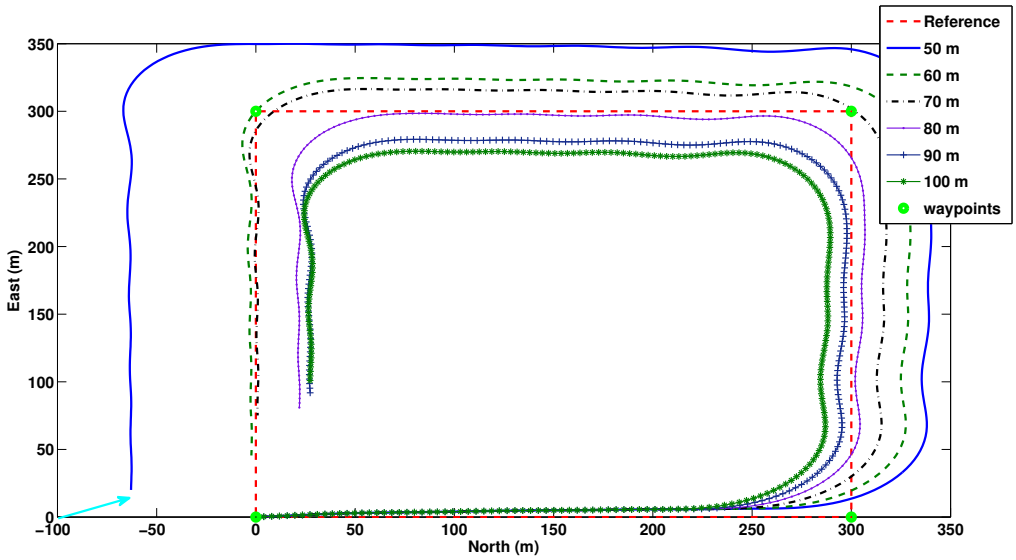

Figure 3.21. Path-specific guidance law sensitivity to waypoint proximity radius.

The sensitivity of the PN guidance law to the is shown in figure 3.22. It is noticed that the smaller the value of the waypoint proximity radius the more flat the airship trajectory tends to be, it is flying an almost rectangular shaped path. As the waypoint proximity radius is increased it is clear that the airship trajectory is more circular in nature; after the first waypoint is passed the airship goes on an ark-like trajectory visiting all the other waypoints in the process. The curvature of the arc increases as the waypoint proximity raduis increases.

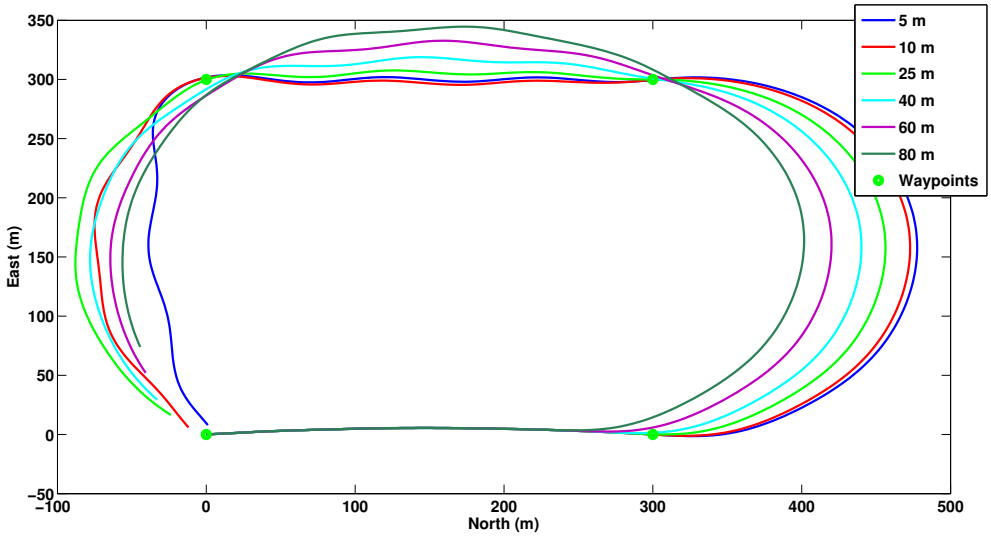

Figure 3.22. PN guidance law sensitivity to waypoint proximity radius.

3.8.4 Scheduling effect case study

A case study is conducted where the simulation for both guidance laws is executed two extra times in zero wind condition, however the value of the scheduling parameter σ was fixed to 1 in one simulation and 0 in the other. This gives the results of the airship flight trajectory when utilizing the straight and level (S-L) model only to control its flight or the level turn (L-T) model only.

It can be deduced from figure 3.23 that for the track-specific guidance law when the (S-L) model is used the flight trajectory is closer to the reference one than that when the (L-T) model is used. When the scheduling law is used however the result is in between the other two results, this is expected for the scheduling law interpolates the gain values based on the parameter σ, and the same argument made earlier about calculating the scheduling parameter σ, through the turn rate, yields a non-zero value of σ for some cases where it should be zero. This is because the value of the turn rate does not go back to a perfect zero after the airship executes its first turn, thereby

causing a deviation on the flight path. The fact that most of the required flight of the airship while flying through the waypoints is in straight and level also explains why the use of the straight and level model only to control the airship yields such results.

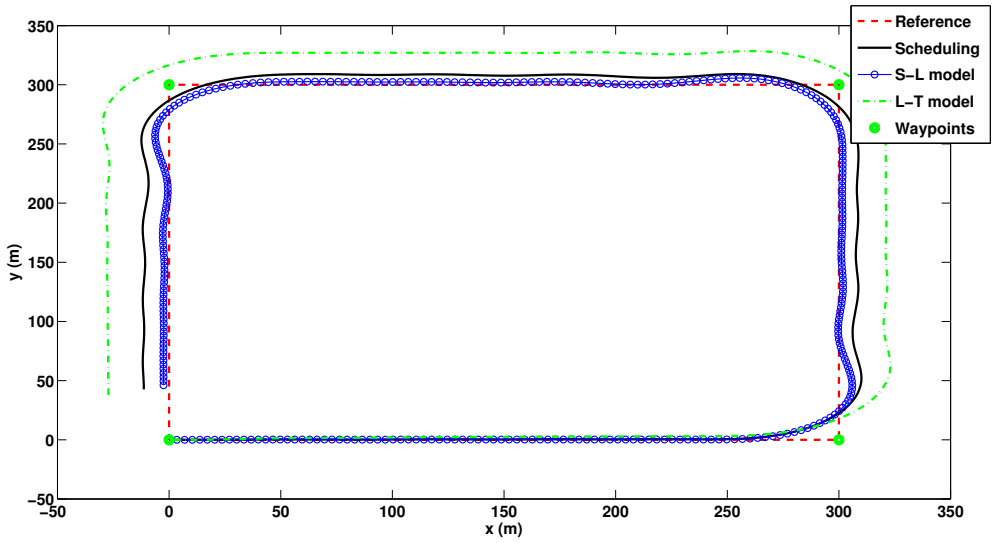

Figure 3.23. Flight trajectories with and without scheduling for track-specific guidance law.

The result for the scheduling case study using the PN guidance law is shown in figure 3.24. The figure shows that the use of a straight and level model only the airship trajectory consists of two straight line segments and two curved segments, together rendering what looks like a racetrack maneuver. However when utilizing the level turn model only the airship trajectory has three curved segments and an almost straight one; this is understandable since the only model available for the controller is a turn model. The result of interest is the one when the scheduling law is used; it is clear that the airship has a most curved trajectory. This is also

attributed to how the scheduling parameter σ is calculated; since in the PN guidance law there is continuously applied lateral acceleration to turn the airship towards the next waypoint, the value of the turn rate after the first waypoint is reached does not go back to zero, this is clear from figure 3.24. Therefore the scheduling parameter is almost never zero for the rest of the simulation which makes the airship exhibit a non-straight, arc-like trajectory while visiting the rest of the waypoints.

Both the controller and guidance laws rely on having all the states of the airship available to function properly. These states however are not always available by measurement, whether the system is built on a budget that doesn't allow for expensive sensors that measure some states, or that some states are not possible to measure with the required accuracy. It can always be assumed that these states are available one way or the other, however the motivation is to make the work presented in this thesis implementable in reality, therefore this problem has to be overcome. The proposed solution for this problem is the design of a Kalman filter algorithm that is capable of optimally estimating the unmeasured states, along with providing an optimal estimate for the measured ones, in order to feedback all the required states by the controller and the guidance algorithm. This topic is discussed in the next chapter.

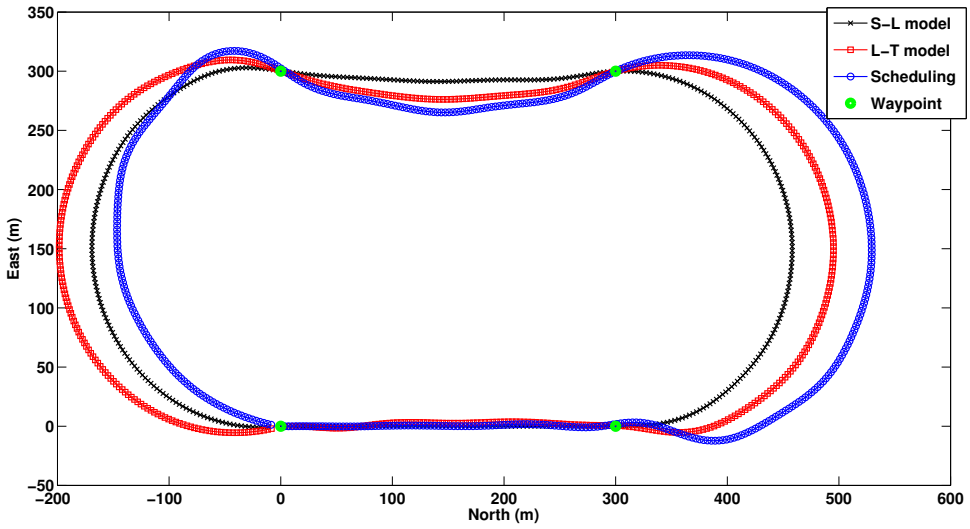

Figure 3.24. Flight trajectories with and without scheduling for proportional navigation guidance law.

CHAPTER 4

STATE AND WIND ESTIMATION

4.1 Introduction

Almost all phenomena we perceive in nature have quantifiable properties. The knowledge of such properties aids in understanding them and the ability to observe them allows for their utilization in the service of mankind. The first attempt of observing a property is usually by measuring it with a sensor that can capture its effect, this measurement however, due to multiple factors which are out of the scope of this thesis, is flawed. The true value of a quantity being measured is never known in practice, the measuring of that quantity gives a corrupted, yet some what accurate observation of the truth. The construction of mathematical models also aids in predicting how a system behaves, therefore giving the ability to again quantify properties of that system which also deviate from the truth. It is often required to obtain the knowledge of a system's properties or states with an accuracy higher than that from measurements and mathematical models. It is sometimes also required to obtain values of unmeasurable states, whether these states are unmeasured due to the lack of sensors to do so, or simply due to the inability to acquire such sensors for any reason such as cost. This is where the Kalman filter has played a significant role in many engineering applications. The Kalman filter is a recursive algorithm capable of optimally estimating a system's states or properties based on a set of observations and a mathematical model of the process.

Different kinds of Kalman filters have been employed in applications spanning from economics [44], computer vision [45, 46], and aerospace applications. Applica-

tions such as State and parameter estimation of aircraft and Unmanned Aerial Vehicles (UAV's) [47, 48, 49, 50], GPS and sensors applications [51, 52], and wind field estimation [53, 54, 24, 55] among many others are all examples of aerospace applications for the Kalman filter. Kalman filters have been utilized in applications involving airships, such as system identification [3] along with parameter and state estimation [56, 57, 58]. The work presented in this chapter will deal with designing an Extended Kalman Filter (EKF), with a minimal sensor suite on-board the airship, for estimating the full state vector of the airship along with the wind field the airship is flying in. It is assumed that no air-data sensors are available, the only sensors available are an IMU and a GPS. A novel Extended Kalman Filter (EKF) is presented, where the Jacobian need not be calculated at every instant, but is precalculated for the different flight modes the airship will carry out. A Jacobian scheduling law is introduced to supply the filter with the needed values at every instant of the flight. This approach reduces computational intensity, since calculating the Jacobian for a complex nonlinear system is a computationally demanding task, without compromising the filters ability to estimate not only the full state vector, but also the bias in measurements and the wind field the airship is flying through. The Kalman filter is implemented for the case where the path-specific guidance law is used to navigate the airship into visiting a set of waypoints. This is because the results presented in subsection 3.8.2 have shown the degradation of performance of the system in the presence of wind, therefore the attempt to estimate wind speeds and supply the path-specific guidance law with such information is carried out to render an optimal wind-estimation based controller.

4.2 The Estimation Process Under a Kalman Filter Framework

There are multiple ways to implement a Kalman filter; the continuous Kalman filter, the discrete Kalman filter, the continuous-discrete Kalman filter and so on. The one more pertaining to reality is the continuous-discrete Kalman filter, it treats the model as a continuous system, which is what real systems are, and the measurements as a discrete process. This holds true because any sensor for it can only supply measurements intermittently at a specific rate. The estimation process based on a linear-continuous-discrete Kalman filter process is described below.

Consider a system model and a measurement model of the following form

$$\begin{aligned} \dot{\mathbf{x}}(t) &= \boldsymbol{A}\mathbf{x}(t) + \boldsymbol{B}\mathbf{u}(t) + \boldsymbol{G}(t)\mathbf{w}(t) \\ \tilde{\mathbf{y}}_k &= \boldsymbol{H}_k\mathbf{x}_k + \mathbf{v}_k \end{aligned} \tag{4.1}$$

where $\mathbf{v}_k$ and $\mathbf{w}(t)$ are the measurement and process noise respectively and are assumed to be zero-mean Gaussian white-noise processes, this implies that the errors are not correlated forward or backward in time [59].

The first step of running a Kalman filter is initializing the estimates and the error covariance matrix, afterwards the Kalman filter works by propagating the state estimates through time based on a mathematical model of the system, the propagated value is denoted as $\hat{\mathbf{x}}_k^-$. When a measurement is observed at some time instant t_k the estimates undergo a discrete time update denoted by $\hat{\mathbf{x}}_k^+$, which are then used as an initial condition to propagate the values to the next time instant t_{k+1} when the next measurement is provided. The error covariance matrix also goes through a propagation and an update by the filter; Since the propagation model is continuous in time the error covariance matrix is propagated by the means of a continuous-time Riccati equation [59], yielding a value $\boldsymbol{P}_k{}^-$. It is also updated based on the standard discrete-time updates, giving the updated value as $\boldsymbol{P}_k{}^+$. The propagation

and update are also termed the predictor and corrector. Below is a summary of the continuous-discrete Kalman filter.

Step 1: Calculating the Kalman gain

$$\boldsymbol{K}_k = \boldsymbol{P}_k{}^{-}\boldsymbol{H}_k{}^{T}[\boldsymbol{H}_k\boldsymbol{P}_k{}^{-}\boldsymbol{H}_k{}^{T} + \boldsymbol{\mathcal{R}}_k]^{-1} \tag{4.2}$$

where $\boldsymbol{\mathcal{R}}$ is the measurement-noise covariance matrix.

Step 2: Update

$$\begin{aligned} \hat{\mathbf{x}}_k^{+} &= \hat{\mathbf{x}}_k^{-} + \boldsymbol{K}_k[\tilde{\mathbf{y}}_k - \boldsymbol{H}_k\hat{\mathbf{x}}_k^{-}] \\ \boldsymbol{P}_k{}^{+} &= [\boldsymbol{I} - \boldsymbol{K}_k\boldsymbol{H}_k]\boldsymbol{P}_k{}^{-} \end{aligned} \tag{4.3}$$

where $\boldsymbol{I}$ is an identity matrix.

Step 3: Propagation

$$\begin{aligned} \dot{\hat{\mathbf{x}}} &= \boldsymbol{F}(t)\hat{\mathbf{x}}(t) + \boldsymbol{B}\mathbf{u}(t) \\ \dot{\boldsymbol{P}}(t) &= \boldsymbol{F}(t)\boldsymbol{P}(t) + \boldsymbol{P}(t)\boldsymbol{F}^{T}(t) + \boldsymbol{G}(t)\boldsymbol{\mathcal{Q}}(t)\boldsymbol{G}^{T}(t) \end{aligned} \tag{4.4}$$

where $\boldsymbol{F}(t)$ is the Jacobian, and $\boldsymbol{\mathcal{Q}}(t)$ is the process-noise covariance matrix.

4.3 The Extended Kalman Filter (EKF)

The Kalman filter introduced in the previous section is based on a linear system model, sadly most systems are of nonlinear nature. To accommodate the nonlinear behavior of real life systems the Extended Kalman Filter (EKF) is utilized. The EKF is one approach among many to represent a linearized version of the Kalman filter [59]. The EKF concept is based on the notion that the true state is adequately close to the estimated state, hence the error dynamics can be approximated by a linearized first-order Taylor series expansion. below is a description of the continuous-discrete EKF.

Assume both the system and measurements behave in a nonlinear fashion as in the following form

$$\begin{aligned} \dot{\mathbf{x}}(t) &= f(\mathbf{x}(t), \mathbf{u}(t), t) + \boldsymbol{G}(t)\mathbf{w}(t) \\ \tilde{\mathbf{y}}_k &= h(\mathbf{x}_k) + \mathbf{v}_k \end{aligned} \tag{4.5}$$

where $\mathbf{v}_k$ and $\mathbf{w}(t)$ are the measurement and process noise respectively and are assumed to be zero-mean Gaussian white-noise processes, along with $f(\mathbf{x}(t), \mathbf{u}(t), t)$ and $h(\mathbf{x}_k)$ being nonlinear functions. To implement an EKF the following steps are to be executed

Step 1: Calculating the Kalman gain

$$\begin{aligned} \boldsymbol{K}_k &= \boldsymbol{P}_k{}^- \boldsymbol{H}_k{}^T(\hat{\mathbf{x}}_k^-)[\boldsymbol{H}_k(\hat{\mathbf{x}}_k^-)\boldsymbol{P}_k{}^- \boldsymbol{H}_k{}^T(\hat{\mathbf{x}}_k^-) + \boldsymbol{\mathcal{R}}_k]^{-1} \\ \boldsymbol{H}_k{}^T(\hat{\mathbf{x}}_k^-) &= \frac{\partial h}{\partial \mathbf{x}}|_{\hat{\mathbf{x}}_k^-} \end{aligned} \tag{4.6}$$

Step 2: Update

$$\begin{aligned} \hat{\mathbf{x}}_k^+ &= \hat{\mathbf{x}}_k^- + \boldsymbol{K}_k[\tilde{\mathbf{y}}_k - h(\hat{\mathbf{x}}_k^-)] \\ \boldsymbol{P}_k{}^+ &= [\boldsymbol{I} - \boldsymbol{K}_k \boldsymbol{H}_k(\hat{\mathbf{x}}_k^-)]\boldsymbol{P}_k{}^- \end{aligned} \tag{4.7}$$

Step 3: Propagation

$$\begin{aligned} \dot{\hat{\mathbf{x}}}(t) &= f(\hat{\mathbf{x}}(t), \mathbf{u}(t), t) \\ \dot{\boldsymbol{P}}(t) &= \boldsymbol{F}(\hat{\mathbf{x}}(t), t)\boldsymbol{P}(t) + \boldsymbol{P}(t)\boldsymbol{F}^T(\hat{\mathbf{x}}(t), t) + \boldsymbol{G}(t)\boldsymbol{\mathcal{Q}}(t)\boldsymbol{G}^T(t) \\ \boldsymbol{F}(\hat{\mathbf{x}}(t), t) &= \frac{\partial f}{\partial \mathbf{x}}|_{\hat{\mathbf{x}}_k} \end{aligned} \tag{4.8}$$

4.4 EKF for Airship State and Wind Speed Estimation

4.4.1 Proccess

When applying the Kalman filter in the scope of this thesis the airship simulated dynamic model derived in chapter 2 will serve as the process. Equation 2.43 rewritten below is the mathematical formulation of the process.

$$\boldsymbol{C_{nss}}\dot{\mathbf{x}} = \boldsymbol{A_{nss}}\mathbf{x} + \boldsymbol{G_{nss}} \tag{4.9}$$

with $\mathbf{x}$ being a twelve state vector expressed as

$$\mathbf{x} = [u \;\; v \;\; w \;\; p \;\; q \;\; r \;\; x \;\; y \;\; z \;\; \phi \;\; \theta \;\; \psi]^T \tag{4.10}$$

4.4.2 Measurements

It is assumed that the airship incorporates two sensors only, a GPS and IMU sensor. The reasoning behind this assumption is to later prove the ability of estimating the entire state vector, measurement bias values, and the wind speed with a minimal number of sensors. Such sensors are available in a conventional suite of on-board UAV avionics [53].

The GPS will provide measurements for the inertial position vector, and the IMU will provide measurements for the angular rates along with the Euler angles. This leads to the following measurement vector

$$\tilde{\mathbf{y}} = [\tilde{p} \;\; \tilde{q} \;\; \tilde{r} \;\; \tilde{x} \;\; \tilde{y} \;\; \tilde{z} \;\; \tilde{\phi} \;\; \tilde{\theta} \;\; \tilde{\psi}]^T \tag{4.11}$$

To synthesize this measurement vector and incorporate it into the airship simulation the values of p ,q ,r ,x ,y ,z ,ϕ ,θ , and ψ from the state vector in 4.10 are corrupted with time-invariant bias and zero-mean Gaussian white-noise. The bias and white-noise standard deviation values are summarized in table 4.1.

4.4.3 Estimate and covariance matrix propagation

- State estimates propagation

For the purpose of propagating the state estimates the same equations used to simulate the airship motion are employed, with the only difference being that the estimated state vector is substituted into the equations as shown below.

$$\boldsymbol{C_{nss}}\dot{\hat{\mathbf{x}}} = \boldsymbol{A_{nss}}\hat{\mathbf{x}} + \boldsymbol{G_{nss}} \tag{4.12}$$

Table 4.1. Standard deviations and bias of measurement vector

Measurement	Standard Deviation	Bias
$\tilde{p}$ (deg/s)	1	2
$\tilde{q}$ (deg/s)	1	2
$\tilde{r}$ (deg/s)	1	2
$\tilde{x}$ (m)	3	0
$\tilde{y}$ (m)	3	0
$\tilde{z}$ (m)	3	0
$\tilde{\phi}$ (deg)	1	0
$\tilde{\theta}$ (deg)	1	0
$\tilde{\psi}$ (deg)	1	0

with $\hat{\mathbf{x}}$ being a twelve state-estimate vector expressed as

$$\hat{\mathbf{x}} = [\hat{u} \;\; \hat{v} \;\; \hat{w} \;\; \hat{p} \;\; \hat{q} \;\; \hat{r} \;\; \hat{x} \;\; \hat{y} \;\; \hat{z} \;\; \hat{\phi} \;\; \hat{\theta} \;\; \hat{\psi}]^T \tag{4.13}$$

- Wind field and measurement bias estimates propagation

To propagate the estimated values of the wind field, the model presented in chapter 2 is utilized. Applying equation 2.48 to the estimates yields the following propagation equations for the wind speed

$$\begin{aligned} \dot{\hat{W}}_x &= -b_w \hat{W}_x \\ \dot{\hat{W}}_y &= -b_w \hat{W}_y \\ \dot{\hat{W}}_z &= 0 \end{aligned} \tag{4.14}$$

and for the wind acceleration

$$\begin{aligned} \ddot{\hat{W}}_x &= -b_w \dot{\hat{W}}_x \\ \ddot{\hat{W}}_y &= -b_w \dot{\hat{W}}_y \\ \ddot{\hat{W}}_z &= 0 \end{aligned} \tag{4.15}$$

As for the bias values to be estimated, since they are time-invariant, the following model for propagating their estimates in time is used

$$\begin{bmatrix} \dot{\hat{b}}_p \\ \dot{\hat{b}}_q \\ \dot{\hat{b}}_r \end{bmatrix} = \begin{bmatrix} 0 \\ 0 \\ 0 \end{bmatrix} \tag{4.16}$$

where $\hat{b}_p, \hat{b}_q$, and $\hat{b}_r$ are the estimated values of the bias in $\tilde{p}$ $\tilde{q}$, and $\tilde{r}$ respectively. The description for the propagation models above leads to an estimates vector of

$$\hat{\mathbf{X}} = [\hat{u} \;\; \hat{v} \;\; \hat{w} \;\; \hat{p} \;\; \hat{q} \;\; \hat{r} \;\; \hat{x} \;\; \hat{y} \;\; \hat{z} \;\; \hat{\phi} \;\; \hat{\theta} \;\; \hat{\psi} \;\; \hat{b}_p \;\; \hat{b}_q \;\; \hat{b}_r \;\; \hat{W}_x \;\; \hat{W}_y \;\; \hat{W}_z \;\; \dot{\hat{W}}_x \;\; \dot{\hat{W}}_y \;\; \dot{\hat{W}}_z]^T \tag{4.17}$$

- Error covariance matrix matrix propagation

The error covariance matrix is an indication of the amount uncertainty of the estimated values. As more knowledge of the state is provided the amount of uncertainty reduces, therefore the covariance matrix is propagated based on the system model and the process noise covariance matrix $\boldsymbol{\mathcal{Q}}$. This is usually done by solving the continuous-time Riccati equation 4.8, however the need to calculate the Jacobian $\boldsymbol{F}(\hat{\mathbf{x}}(t), t) = \frac{\partial f}{\partial \mathbf{x}}|_{\hat{\mathbf{x}}_k}$ at every instant is computationally expensive, and can be a complicated process for highly nonlinear systems. As a solution to this problem the Jacobian for the two linear systems derived in chapter 3, extended to incorporate elements for the bias terms and wind terms to be estimated, is implemented in the error covariance matrix propagation. The two augmented Jacobians are then scheduled with the scheduling law proposed for the controller gains presented in equation 3.10, then a value of the Jacobian at every flight condition is supplied to the filter, by the scheduling law, for the purpose of propagating the error covariance matrix.

In this novel implementation of the EKF only 6 elements out of the total 441 in the Jacobian are required to be calculated at every instant, these elements are the ones pertaining to the change of the linear velocities ($u \quad v \quad w$) and angular rates

$(p \quad q \quad r)$ with respect to the wind acceleration. This effect can be seen in equations 2.41 and 2.42. The Jacobians for straight and level flight and level turn flight are

$$\boldsymbol{F}_{SL} = \begin{bmatrix} \boldsymbol{A}_{SL} & [\boldsymbol{0}]_{3\times3} & [\boldsymbol{0}]_{3\times3} & [\frac{d\mathbf{V}}{d\dot{\mathbf{W}}}] \\ [\boldsymbol{0}]_{3\times3} & [\boldsymbol{0}]_{3\times3} & [\boldsymbol{0}]_{3\times3} & [\frac{d\boldsymbol{\omega}}{d\dot{\mathbf{W}}}] \\ [\boldsymbol{0}]_{3\times3} & [\boldsymbol{0}]_{3\times3} & \boldsymbol{I}_{3\times3} & [\boldsymbol{0}]_{3\times3} \\ [\boldsymbol{0}]_{3\times3} & [\boldsymbol{0}]_{3\times3} & [\boldsymbol{0}]_{3\times3} & [\boldsymbol{0}]_{3\times3} \\ [\boldsymbol{0}]_{3\times3} & [\boldsymbol{0}]_{3\times3} & [\boldsymbol{0}]_{3\times3} & [\boldsymbol{0}]_{3\times3} \\ [\boldsymbol{0}]_{3\times3} & [\boldsymbol{0}]_{3\times3} & [\boldsymbol{B_w}] & [\boldsymbol{0}]_{3\times3} \\ [\boldsymbol{0}]_{3\times3} & [\boldsymbol{0}]_{3\times3} & [\boldsymbol{0}]_{3\times3} & [\boldsymbol{B_w}] \end{bmatrix} \tag{4.18}$$

$$\boldsymbol{F}_{LT} = \begin{bmatrix} \boldsymbol{A}_{LT} & [\boldsymbol{0}]_{3\times3} & [\boldsymbol{0}]_{3\times3} & [\frac{d\mathbf{V}}{d\dot{\mathbf{W}}}] \\ [\boldsymbol{0}]_{3\times3} & [\boldsymbol{0}]_{3\times3} & [\boldsymbol{0}]_{3\times3} & [\frac{d\boldsymbol{\omega}}{d\dot{\mathbf{W}}}] \\ [\boldsymbol{0}]_{3\times3} & [\boldsymbol{0}]_{3\times3} & \boldsymbol{I}_{3\times3} & [\boldsymbol{0}]_{3\times3} \\ [\boldsymbol{0}]_{3\times3} & [\boldsymbol{0}]_{3\times3} & [\boldsymbol{0}]_{3\times3} & [\boldsymbol{0}]_{3\times3} \\ [\boldsymbol{0}]_{3\times3} & [\boldsymbol{0}]_{3\times3} & [\boldsymbol{0}]_{3\times3} & [\boldsymbol{0}]_{3\times3} \\ [\boldsymbol{0}]_{3\times3} & [\boldsymbol{0}]_{3\times3} & [\boldsymbol{B_w}] & [\boldsymbol{0}]_{3\times3} \\ [\boldsymbol{0}]_{3\times3} & [\boldsymbol{0}]_{3\times3} & [\boldsymbol{0}]_{3\times3} & [\boldsymbol{B_w}] \end{bmatrix} \tag{4.19}$$

where $[\frac{d\mathbf{V}}{d\dot{\mathbf{W}}}]$ and $[\frac{d\boldsymbol{\omega}}{d\dot{\mathbf{W}}}]$ are the Jacobians for equations 2.41 and 2.42 respectively and

$$[\boldsymbol{B_w}] = \begin{bmatrix} -b_w & 0 & 0 \\ 0 & -bw & 0 \\ 0 & 0 & 0 \end{bmatrix} \tag{4.20}$$

The following scheduling law is used to acquire the value of the Jacobian

$$\boldsymbol{F} = (1-\sigma)\boldsymbol{F}_{SL} + \sigma\boldsymbol{F}_{LT} \tag{4.21}$$

where σ is the same scheduling parameter presented in chapter 3. Now to propagate the error covariance matrix the continuous-time Riccati equation equation is solved as follows

$$\dot{\boldsymbol{P}}(t) = \boldsymbol{F}\boldsymbol{P}(t) + \boldsymbol{P}(t)\boldsymbol{F}^T + \boldsymbol{G}\boldsymbol{\mathcal{Q}}\boldsymbol{G}^T \tag{4.22}$$

where $\boldsymbol{\mathcal{Q}}$ is an 15 by 15 diagonal matrix with the following diagonal elements

$\boldsymbol{\mathcal{Q}}_{i,i}$	Value	$\boldsymbol{\mathcal{Q}}_{i,i}$	Value
$\boldsymbol{\mathcal{Q}}_{1,1}$	1e-2	$\boldsymbol{\mathcal{Q}}_{9,9}$	1e-6
$\boldsymbol{\mathcal{Q}}_{2,2}$	1e-2	$\boldsymbol{\mathcal{Q}}_{10,10}$	1e-6
$\boldsymbol{\mathcal{Q}}_{3,3}$	1e-2	$\boldsymbol{\mathcal{Q}}_{11,11}$	1e-6
$\boldsymbol{\mathcal{Q}}_{4,4}$	1e-2	$\boldsymbol{\mathcal{Q}}_{12,12}$	1e-6
$\boldsymbol{\mathcal{Q}}_{5,5}$	1e-2	$\boldsymbol{\mathcal{Q}}_{13,13}$	1e-6
$\boldsymbol{\mathcal{Q}}_{6,6}$	1e-2	$\boldsymbol{\mathcal{Q}}_{14,14}$	1e-6
$\boldsymbol{\mathcal{Q}}_{7,7}$	1e-6	$\boldsymbol{\mathcal{Q}}_{15,15}$	1e-6
$\boldsymbol{\mathcal{Q}}_{8,8}$	1e-6	-	-

and

$$\boldsymbol{G} = \begin{bmatrix} \boldsymbol{I}_{\mathbf{6\times 15}} \\ [\mathbf{0}]_{\mathbf{6\times 15}} \\ [[\mathbf{0}]_{\mathbf{3\times 6}} \;\; \boldsymbol{I}_{\mathbf{3\times 3}} \;\; [\mathbf{0}]_{\mathbf{3\times 6}}] \\ [[\mathbf{0}]_{\mathbf{3\times 9}} \;\; \boldsymbol{I}_{\mathbf{6\times 6}}] \end{bmatrix} \tag{4.23}$$

4.4.4 Estimate and covariance matrix update

The update phase of the EKF is implemented every time a measurement is available, this is done by first calculating the Kalman gain from equation 4.6 however here the Jacobian ${\boldsymbol{H}_k}^T(\hat{\mathbf{x}}_k^-) = \frac{\partial h}{\partial \mathbf{x}}|_{\hat{\mathbf{x}}_k^-}$ has a constant value for all flight. This is due to the fact that there is no explicit measurement model, since the measurements

are generated by corrupting the states from the process with zero-mean Gaussian white-noise. The Kalman gain is calculated as

$$\boldsymbol{K}_k = \boldsymbol{P}_k{}^{-}\boldsymbol{H}^T[\boldsymbol{H}\boldsymbol{P}_k{}^{-}\boldsymbol{H}^T + \boldsymbol{\mathcal{R}}_k]^{-1} \tag{4.24}$$

with $\boldsymbol{\mathcal{R}}_k$ being a 9 by 9 diagonal matrix with the following elements guidance

algorithm

$\boldsymbol{\mathcal{R}}_{i,i}$	Value	$\boldsymbol{\mathcal{R}}_{i,i}$	Value	$\boldsymbol{\mathcal{R}}_{ii}$	Value
$\boldsymbol{\mathcal{R}}_{1,1}$	$(\pi/180)^2$	$\boldsymbol{\mathcal{R}}_{4,4}$	3^2	$\boldsymbol{\mathcal{R}}_{7,7}$	$(\pi/180)^2$
$\boldsymbol{\mathcal{R}}_{2,2}$	$(\pi/180)^2$	$\boldsymbol{\mathcal{R}}_{5,5}$	3^2	$\boldsymbol{\mathcal{R}}_{8,8}$	$(\pi/180)^2$
$\boldsymbol{\mathcal{R}}_{3,3}$	$(\pi/180)^2$	$\boldsymbol{\mathcal{R}}_{6,6}$	3^2	$\boldsymbol{\mathcal{R}}_{9,c9}$	$(\pi/180)^2$

and

$$\boldsymbol{H} = \begin{bmatrix} [\boldsymbol{0}]_{\boldsymbol{3\times 3}} & [\boldsymbol{I}]_{\boldsymbol{3\times 3}} & [\boldsymbol{0}]_{\boldsymbol{3\times 6}} & [\boldsymbol{I}]_{\boldsymbol{3\times 3}} & [\boldsymbol{0}]_{\boldsymbol{3\times 6}} \\ [\boldsymbol{0}]_{\boldsymbol{3\times 6}} & [\boldsymbol{I}]_{\boldsymbol{3\times 3}} & [\boldsymbol{0}]_{\boldsymbol{3\times 4}} & [\boldsymbol{0}]_{\boldsymbol{3\times 4}} & [\boldsymbol{0}]_{\boldsymbol{3\times 4}} \\ [\boldsymbol{0}]_{\boldsymbol{3\times 9}} & [\boldsymbol{I}]_{\boldsymbol{3\times 3}} & [\boldsymbol{0}]_{\boldsymbol{3\times 3}} & [\boldsymbol{0}]_{\boldsymbol{3\times 3}} & [\boldsymbol{0}]_{\boldsymbol{3\times 3}} \end{bmatrix}$$

After the Kalman gain has been calculated the estimate vector and the error covariance matrix are updates as follows

$$\begin{aligned} \hat{\mathbf{X}}_k^+ &= \hat{\mathbf{X}}_k^- + \boldsymbol{K}_k[\tilde{\mathbf{y}}_k - \hat{\mathbf{y}}(\hat{\mathbf{X}}_k^-)] \\ \boldsymbol{P}_k{}^+ &= [\boldsymbol{I} - \boldsymbol{K}_k\boldsymbol{H}_k(\hat{X}_k^-)]\boldsymbol{P}_k{}^- \end{aligned} \tag{4.25}$$

where

$$\hat{\mathbf{y}}(\hat{\mathbf{X}}_k^-) = [\hat{p}\ \ \hat{q}\ \ \hat{r}\ \ \hat{x}\ \ \hat{y}\ \ \hat{z}\ \ \hat{\phi}\ \ \hat{\theta}\ \ \hat{\psi}]^T \tag{4.26}$$

and $\hat{\mathbf{X}}_k^-$ is the propagated estimate vector in 4.17, and $\boldsymbol{P}_k{}^-$ is the propagated value of the error covariance matrix at the previous instant.

The estimate vector is fed back to the guidance algorithm and the controller in order to fly the airship, in the presence of wind, through all the waypoints. It is again reminded that the goal is to make the airship visit all the waypoints in the order they are given.

4.5 Results and Discussion

4.5.1 Flight with no wind

A simulation, with similar conditions to the one who's results are displayed in section 3.8, is conducted to show the performance of the controller when the estimated state vector is given as feedback instead of the actual state vector. Some design parameters have to be altered, this is attributed to the level of uncertainty in the estimated states, this affects the controller performance. The waypoint proximity zone radius is kept at 60 m, however the design parameter τ in the guidance law is changed to 60 instead of 10 to yield satisfactory results. Two main simulations are conducted, one in zero wind conditions and another under the influence of the same wind field shown in section 3.8. The latter was simulated twice, where in one run the estimated values of the wind field were not fed to the guidance algorithm, unlike the second run where the estimated values of the wind field were known to the guidance algorithm. The results are presented here to show how a more realistic scenario can be implemented to navigate the airship from one waypoint to the other in the presence of wind disturbance.

Figures 4.1 to 4.5 show the error between the estimated value and true value of each state along with the bias, and figure 4.6 shows the true and estimated values of the bias in the angular rates measurements. The 3-σ bounds are also plotted on these figures, these bounds dictate the tolerance an estimation error is allowed to have. The σ bounds are an indication to the maximum uncertainty allowed in the estimated values, they are extracted from the error covariance matrix. There is only so much information available to the filter, which limits its ability of estimating the true values. It can be seen from these figures that the error values for all estimates are well within the limit of the 3-σ bounds, that is an indication that the filter is

working properly. The value if the 3-σ bound in figures 4.2, 4.3, and 4.4 are slightly less than three times that of the standard deviations in table 4.1 used to generate their measurements. The 3-σ bound for the angular rates estimates is 2.85 deg/s, for the inertial position 8.8 m, and for the Euler angles 2.9 deg. This indicates that the estimates are slightly closer to the truth value from that of the measurements. The more important result however is seen in figures 4.1 and 4.5; the value of the 3-σ bound for the body axis velocity components is less than 0.6 m, and the value for 3-σ bound of the bias value estimates is less than 1 deg. This shows the ability to estimate the values of unmeasured states and bias with a low uncertainty.

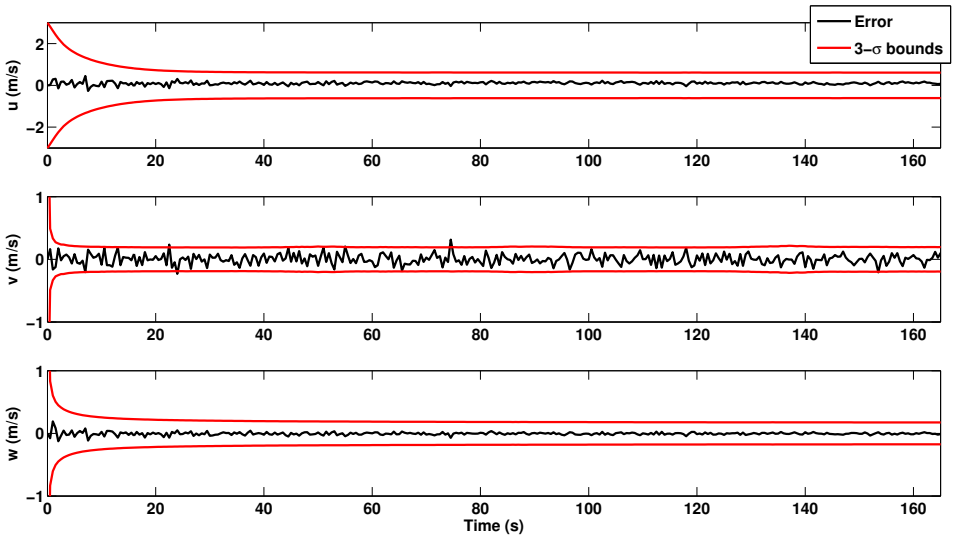

Figure 4.1. The estimation error and 3-σ bounds of the body-axes velocity components in no wind condition.

Figures 4.7 to 4.10 and 4.12 are very similar to the results shown in the previous chapter when the true values of the states were fed back to the controller, however figure 4.11 shows the difference in performance if compared to the result in figure

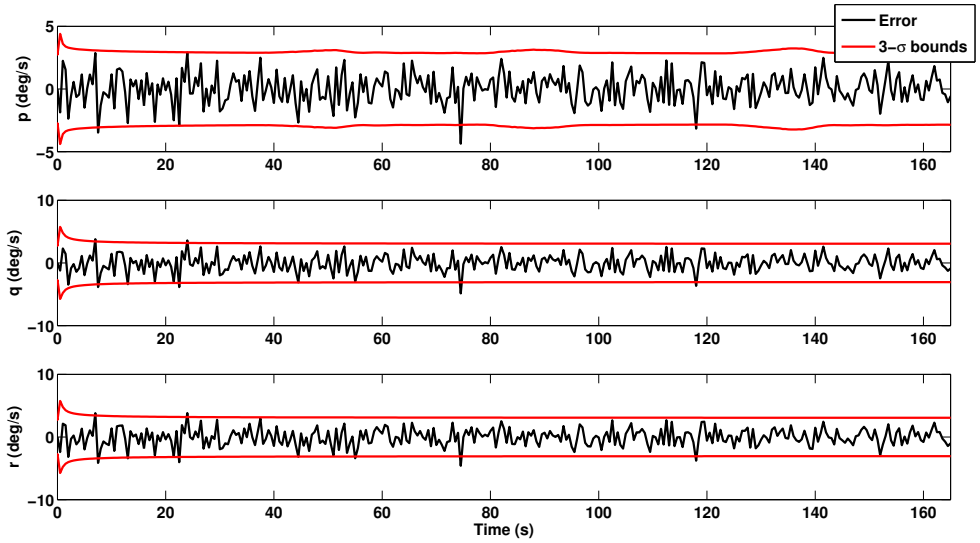

Figure 4.2. The estimation error and 3-σ bounds of the body-axes angular rates in no wind condition.

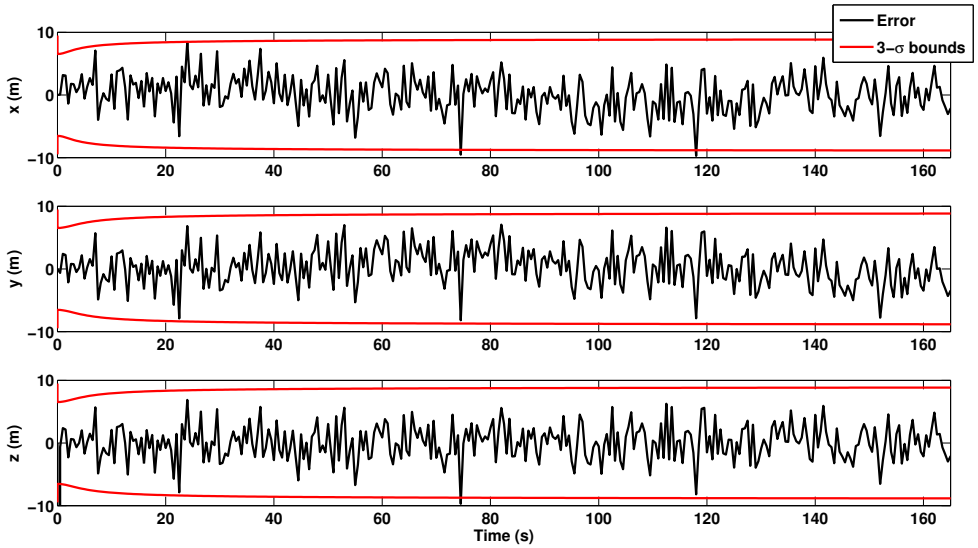

Figure 4.3. The estimation error and 3-σ bounds of the airship inertial position in no wind condition.

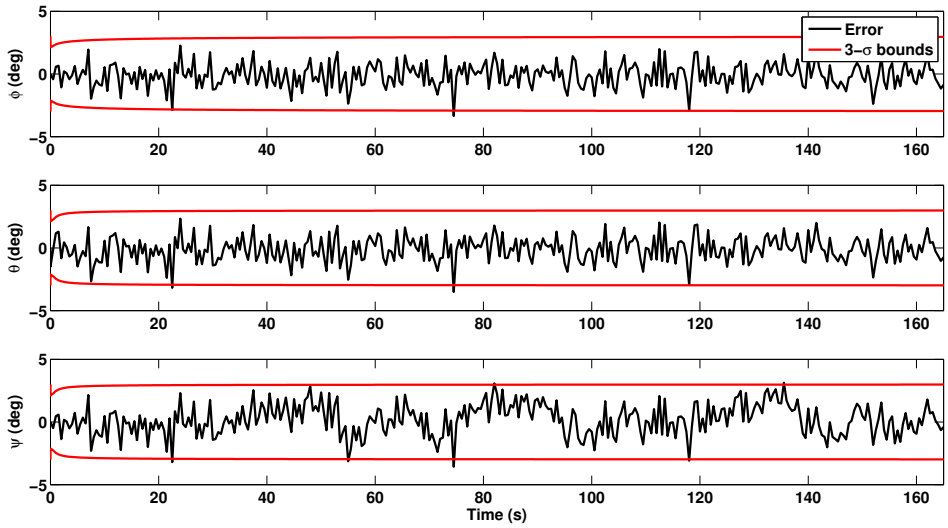

Figure 4.4. The estimation error and 3-σ bounds of the airship attitude in no wind condition.

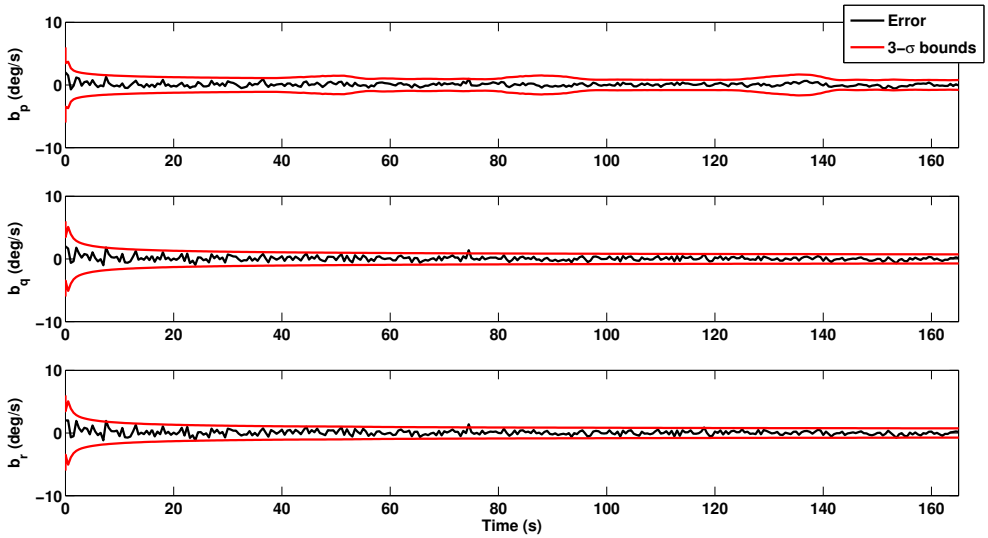

Figure 4.5. The estimation error and 3-σ bounds of bias in $\tilde{p}$, $\tilde{q}$, and $\tilde{r}$ respectively in no wind condition.

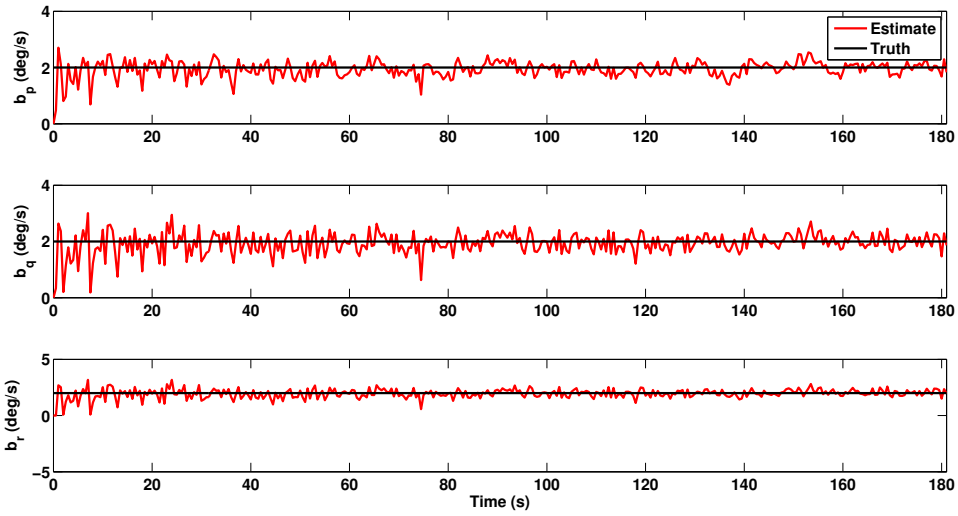

Figure 4.6. True and estimated values of bias in $\tilde{p}$, $\tilde{q}$, and $\tilde{r}$ respectively in no wind condition.

3.17. This change in performance is understandable for the values of the estimated states have an uncertainty which deviates the controllers performance from that when the true states where used in the feedback process. The maximum deviation from the reference trajectory is 21.7 m, and occurs in the fourth segment.

4.5.2 Flight in the presence of wind

The same simulation carried out in subsection 3.8.2, with the presence of the same wind field condition and with feedback of the estimated states. Here however, the simulation is executed twice; during the first time estimated wind speeds are fed to the navigation algorithm, and the second time they are not. When the estimated wind speeds are known to the navigation algorithm, it is capable of generating desired heading angle signals that ensure better performance of the controller. Figure 4.14 shows the estimation error and the 3-σ bounds of the wind speed, while figure 4.13

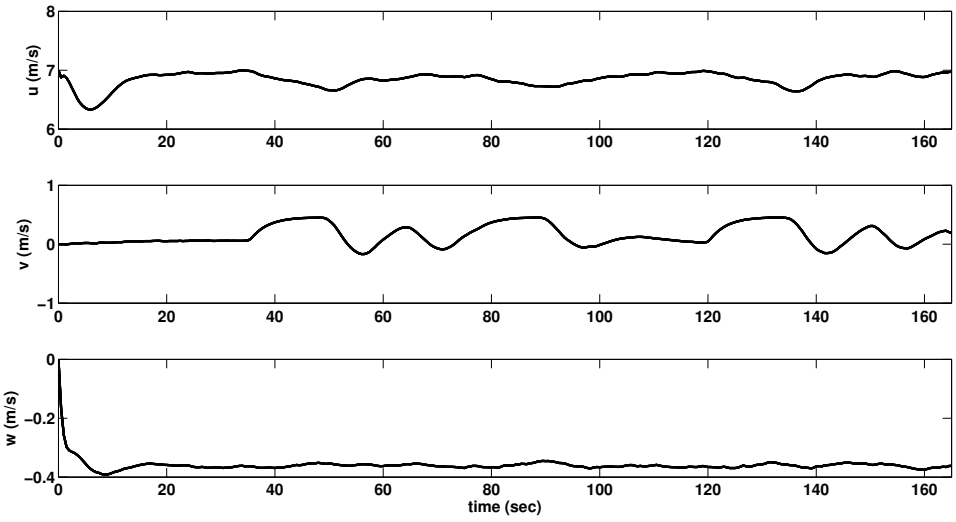

Figure 4.7. Time history of body-axes velocity components for controller performance with estimated states feedback in no wind condition.

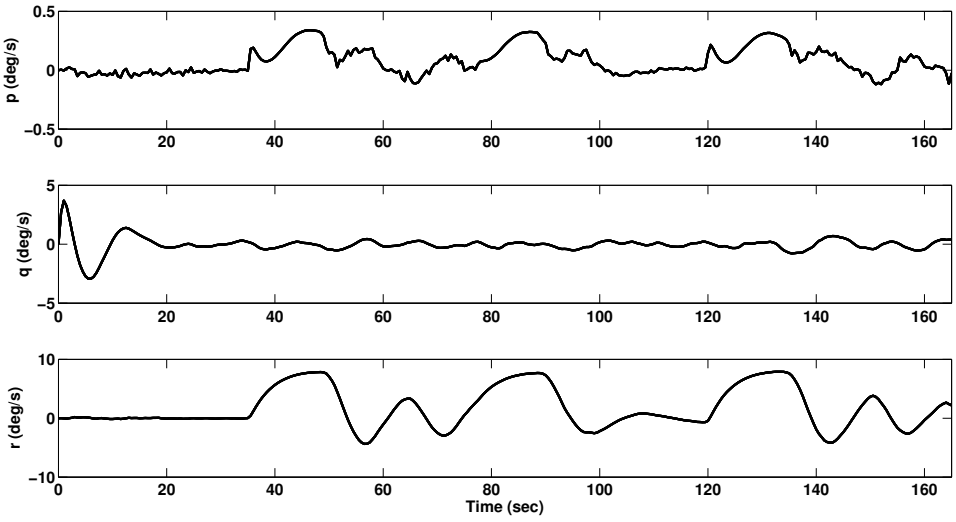

Figure 4.8. Time history of body-axes angular rates for controller performance with estimated states feedback in no wind condition.

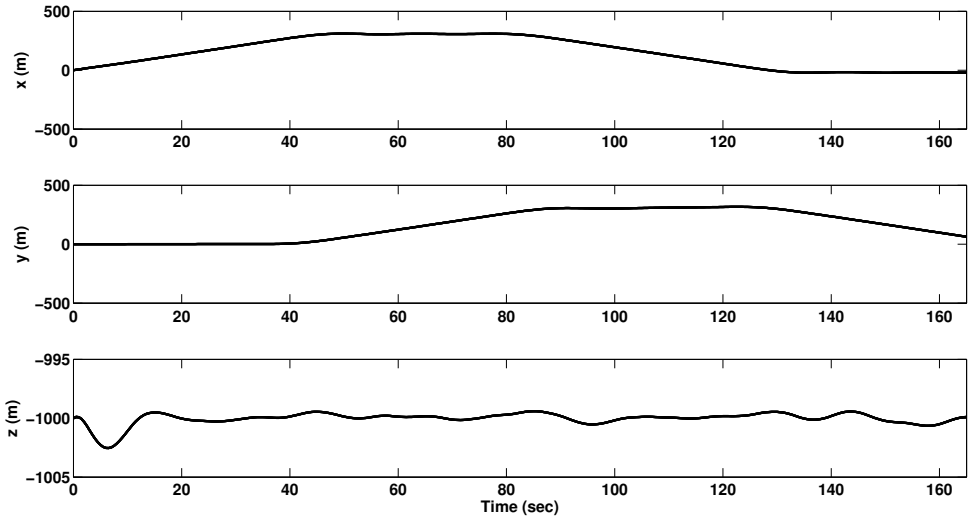

Figure 4.9. Time history of airship inertial position for controller performance with estimated states feedback in no wind condition.

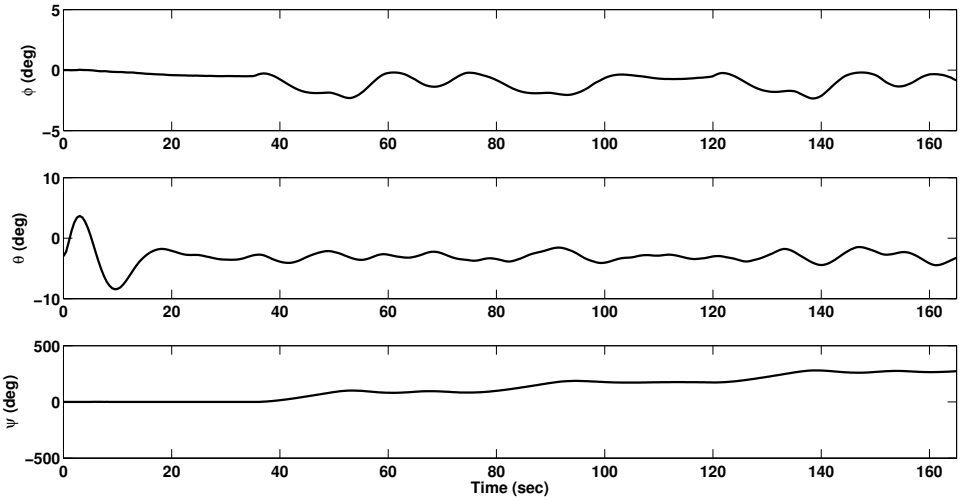

Figure 4.10. Time history of airship attitude for controller performance with estimated states feedback in no wind condition.

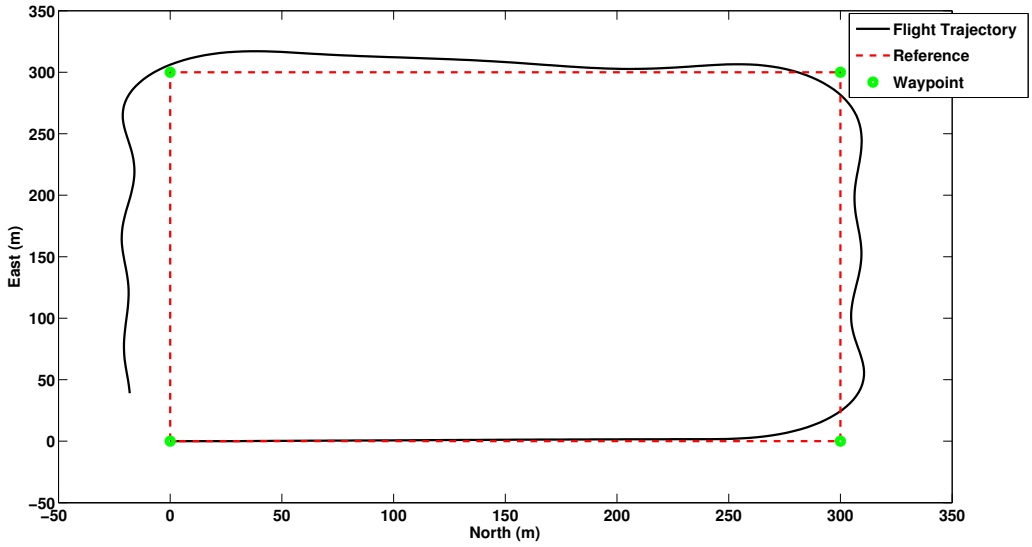

Figure 4.11. Airship flight path for controller performance with estimated states feedback in no wind condition.

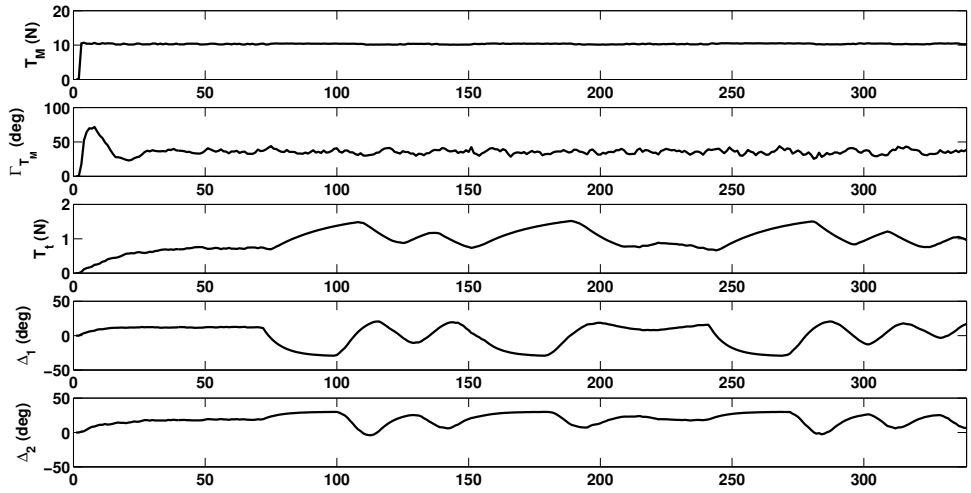

Figure 4.12. Airship control inputs for controller performance with estimated states feedback in no wind condition.

shows the true and estimated values of the wind speeds. It is clear that the Kalman filter is capable of estimating the wind speed with acceptable levels of uncertainty, given the minimal number of sensors on-board the airship.

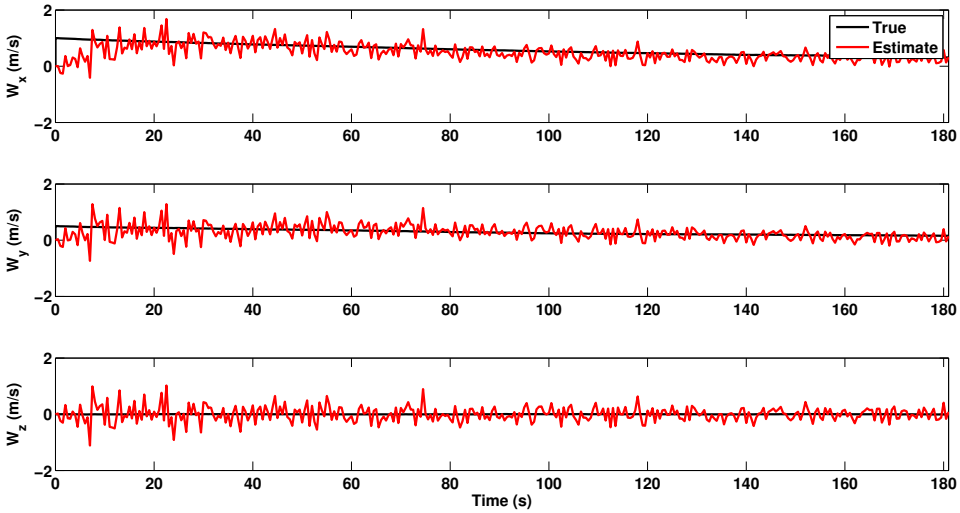

Figure 4.13. True and estimated value of wind speeds.

4.5.3 Wind-estimation based control

The design and implementation of the EKF with a minimal number of sensors has aided in estimating the wind field in which the airship is flying. This information can now be used to render the controller and TS guidance law more robust to wind. The value of the estimated wind speeds are fed into the TS guidance law in such a way that the inertial velocities used to calculate the vehicle heading in equation 3.22, account for the wind information. This enables the TS guidance law to generate more robust signals to the controller which in turn supplies the control commands required to enhance the airship performance in the presence of wind. Examining figure 4.15

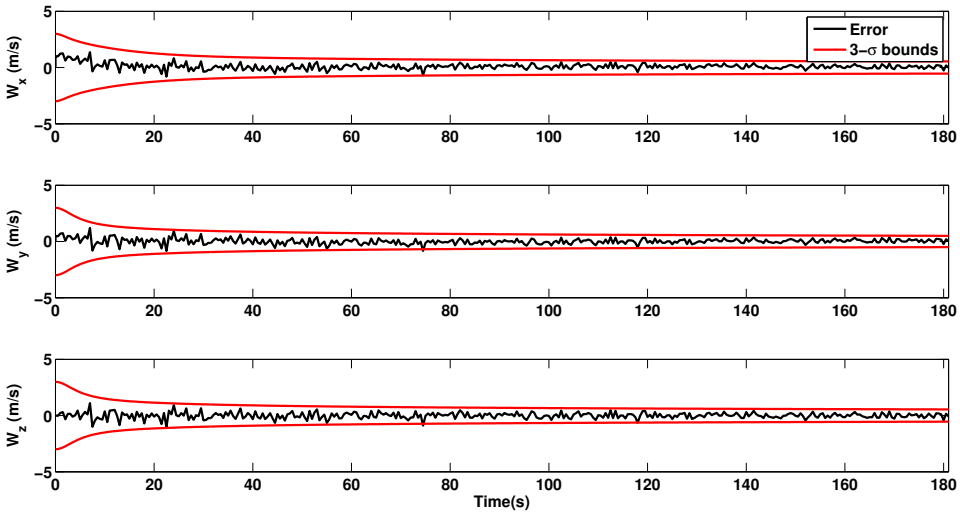

Figure 4.14. The estimation error and 3-σ bounds of wind speed.

it can be seen that in both simulation cases the TS guidance law is robust to wind, however, this robustness is amplified when the estimated wind speeds are available at its disposal. The maximum deviation from the reference trajectory when wind information is not supplied to the TS guidance law is 67.1 m, occurring in the third segment. The maximum deviation is reduced to 47.1 m when the estimated wind speeds are provided to the TS guidance law.

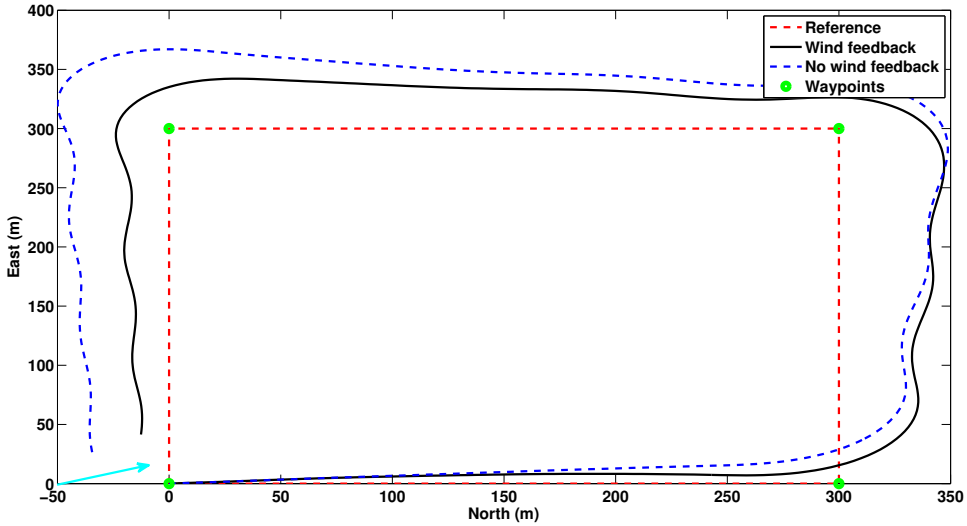

Figure 4.15. Flight trajectories with and without wind speed estimate feedback under the influence of North-East wind.

CHAPTER 5

CONCLUDING REMARKS AND FUTURE WORK

5.1 Thesis contribution

With growing demand on applications requiring long endurance hover, in both the civil and military applications, and the airship being a viable option for such applications, the need to control such vehicles with a certain accuracy related to realistic flight environment is essential. This thesis relied on the AS500 unmanned airship model, which has been utilized for many applications, to address this need. The work presented in this thesis consisted of three major parts, all listed below

- Constructing a nonlinear mathematical model for simulating an unmanned airship flight.
- Designing optimal controllers using the LQR and LQI methods, along with two guidance laws to accommodate each controller and navigate the airship through waypoints.
- Design and implement a novel EKF to the airship control simulation.

The first major contribution of this thesis is the implementation of a novel EKF where the Jacobian need not be calculated at every instant of the simulation, but rather having precaculated ones and acquire the needed values based on a scheduling law, without compromising the filters ability to estimate the airship states, measurement bias, and surrounding wind speeds with a minimal number of sensors.

The second major contribution of this thesis is proving the fact that the estimated wind speeds, provided by the EKF, allow increased robustness of the path-specific guidance law and LQR control law to wind. It was shown that the airship

has higher performance when the wind speed information from the EKF is passed to the guidance algorithm.

The thesis also contributed to establishing a clear difference between the logic employed by the path-specific guidance law and the PN law. Where the first was more focused on flying the airship on a prescribed trajectory to reach each waypoint, while the second was more concerned in achieving each waypoint without any consideration to a specific trajectory. It was also established that the PN guidance law was able to meet more strict requirements for buffer zone radius where it was able to visit all waypoints with a buffer radius of 5 m under the defined wind condition, unlike the path-specific guidance law which was capable of visiting all waypoints at a minimum radius of 50 m under the same wind condition.

It is clear from the results presented in this thesis that the guidance laws presented along with the proposed controllers, are capable of flying the airship in a stable manner to visit a set of waypoints. It has been demonstrated that the presence of wind decreases the robustness of the path-specific guidance law and control scheme presented. The PN guidance law presented showed high robustness to wind and capability to visit each waypoint at a small buffer radius requirement. It was also proved possible to run a less computationally expensive Extended Kalman filter, based on Jacobian scheduling, with the minimum amount of sensors available on an airship to estimate the entire airship state vector, measurement bias, and wind speeds with an acceptable level of uncertainty. And finally it was shown that when the estimated values of wind speeds were supplied to the guidance algorithm its robustness to wind was enhanced.

5.2 Future Work

The work presented in this thesis lays the groundwork for creating a simulation environment for the AS500 airship capable of accommodating different control and navigation schemes. The control and scheduling law accompanied by a navigation laws and a Kalman filter have shown the ability to navigate the airship through a series of waypoints. Several other studies can be augmented to the developed simulation environment rendering it a test bed for guidance, navigation, and control of airships. Some future studies that can be implemented include:

- Expanding the current controller capabilities to include a hover operating point with station-keeping abilities.
- Designing and implementing an adaptive control scheme to control the airship flight, including a hover operating point, to enhance performance.
- Studying the feasibility of utilizing an airship fleet for surrogate GPS applications.

5.3 Final Words

The airship, as a useful multipurpose atmospheric flight vehicle, has been abandoned in the past for safety reasons. The work conducted by researchers and engineers for the past decade accompanied by the work presented in this document, show that with the advancement of many scientific fields, especially control and estimation theory, it is possible to feasibly and safely operate a manned or unmanned airship. The airship platform can be utilized for many applications where conventional aircraft designs are either inapplicable, or too expensive. The airship can also serve as an alternative to some space vehicle applications at a much lower cost, such as GPS satellites. With all the facts presented it cannot be denied that the airship is vital

to the advancement of aerospace technologies, as well as many other fields such as communications and meteorology, therefore contributions to research in airships is crucial.

REFERENCES

[1] Li, Y., "Dynamics Modeling and Simulation of Flexible Airships," PhD Thesis, Department of Mechanical Engineering, McGill University, Montreal, Quebec, Canada, 2008.

[2] Gerken, L. C., *Airships: History and Technology*, AmeraTechReportican Scientific Corp., Chula Vista, CA, 1990.

[3] Kornienko, A., "System Identification Approach for Determining Flight Dynamical Characteristics of an Airship from Flight Data," Doctor of Engineering Dissertation, Faculty of Aeronautics and Astronautics and Geodesy, University of Stuttgart, Stuttgart, Germany, 2008.

[4] Mueller, J. and Paluszek, M., "Development of an Aerodynamic Model and Control Law Design for a High Altitude Airship," *3rd Unmanned Unlimited Technical Conference, Workshop and Exhibit*, AIAA, Chicago, Illinois, 2004.

[5] Bueno, S., Azinheira, J., Ramos, J., Paiva, E., Rives, P., Elfes, A., Carvalho, J., , and Silveira, G., "Project AURORA: Towards an Autonomous Robotic Airship," *International Conference on Intelligent Robots and Systems*, IEEE/RSJ, Lausanne, Switzerland, 2002.

[6] Khoury G., A. and Gillett J., D., *Airship technology*, Cambridge University Press, Cambridge, United Kingdom, 2004.

[7] Lacroix, S. and Jung, I. K., "High Resolution Terrain Mapping with an Autonomous Blimp," *Proceedings of the International Conference onIntelligent Robots and Systems*, IEEE/RSJ, Luasanne, Switzerland, 2002.

[8] Hygounenc, E., Jung, I. K., Soueres, P., and Lacroix, S., "The Autonomous Blimp Project of LAAS-CNRS: Achievements in Flight Control and Terrain Mapping," *The International Journal of Robotics Research*, Vol. 23, No. 4, 2004.

[9] Waishek, J., Dogan, A., and Bestaoui, Y., "Investigation into the Time Varying Mass Effect on Airship Dynamics Response," *Proceedings of Aerospace Sciences Meeting Including th New Horizons Forum and Aerospace Exposition*, AIAA, Orlando, Florida, 2009.

[10] Waishek, J. and Dogan, A., "Comprehensive Characterization of Airship Response to Wind and Time Varying Mass," *Proceedings of Atmospheric Flight Mechanics Conference*, AIAA, Toronto, Ontario Canada, 2010.

[11] Waishek, J., "Derivation of the Dynamics Equations for an Aircraft in Aerial Refueling," M.S Thesis, Department of Mechanical and Aerospace Engineering, The University of Texas at Arlington, Arlington, Texas, USA, 2007.

[12] Dogan, A., "AE 5302 - Advanced Flight Mechanics," *Lecture Notes*, 2010.

[13] M.Munk, M., "Notes on Aerodynamic Forces - II Curvilinear Motion," Tech. rep., NACA, Report Number 105, July, 11 1924.

[14] L., B., T., "Notes on Aerodynamic Forces on Airship hulls," Tech. rep., NACA, Report Number 129 March, 10 1923.

[15] M.Munk, M., "The Aerodynamic Forces on Airship Hulls," Tech. rep., NACA, Report Number 184 1922.

[16] Upson, R. and Klikoff, W., "Application to Practical Aerodynamics to Airship Design," Tech. rep., NACA, June, 1 1931.

[17] Jones, S. and DeLaurier, J., "Aerodynamic Estimation Techniques for aerostates and airships," *Proceedings Lighter-than-air Systems Conference*, AIAA, Annapolis, Md, 1982.

[18] Shields, K., "CFD Applications in Airship Design," M.S. Thesis, Department of Mechanical Engineering, West Virginia University, Morgantown, West Virginia, USA, 2010.

[19] Gomes, S., B. V., "An Investigation of the Flight Dynamics of Airships with Application to the YEZ-2A," PhD Thesis, Aeronautics Department, Cranfield Institute of Technology,Cranfield, United Kingdom 1990.

[20] Zhao, Y., Gerrard, W., and Mueller, J., "Benefits of Trajectory Optimization in Airship Flight," *Proceedings of the 3rd Unmanned Unlimited Technical Conference, Workshop and Exhibit*, AIAA, Chicago, Illinois, 2004.

[21] Frye, M., Gammon, S., and Qian, C., "The 6-DOF Dynamic Model and Simulation of the Tri-Turbofan Remote-Controlled Airship," *Proceedings of the American Control Conference*, IEEE, New York City, New York, USA, 2007.

[22] WU, X., Moog, C., and Hu, Y., "Modeling and Linear Control of a Buoyancy-Driven Airship," *Proceedings of the Asian Control Conference*, IEEE, Hong Kong, 2009.

[23] Ashraf, Z. and Choudhry, M., "Dynamic Modeling of the Airship Using Analytical Aerodynamic Model," *Proceedings of the International Conference on Emerging Technologies*, IEEE, Islamabad, Pakistan, 2009.

[24] Je Hyeon Lee, A. D. and Hullender, D., "Estimation of Aircraft States and Wind Exposure," *Proceedings of the Guidance, Navigation, and Control Conference*, AIAA, Portland, Oregon, USA, 2011.

[25] De Paiva, E., C. Bueno, S., Gomes, S., B. V., Ramos, J., J. G., and Bergerman, M., "A Control System Development Environment for AURORAs Semi-Autonomous Robotic Airship," *Proceedings of the International Conference on Robotics and Automation*, IEEE, Demit, Michigan, USA, 1999.

[26] Carvalho, J., De Paiva, E., Azinheira, J., Ferreira, P., Ramos, J., Bueno, S., Bergerman, M., Maeta, S., Mirisola, L., Faria, B., and Elfes, A., "Classic and Robust PID Heading Control of an Unmanned Robotic Airship," *Proceedings of the 9th international symposium on intelligent robotic systems*, Toulouse, France, 2001.

[27] Park, C.-S., Lee, H., Tahk, M.-J., and Bang, H., "Airship Control Using Neural Network Augmented Model Inversion," *Proceedings of the Conference on Control Applications*, Istanbul, Turkey, 2003.

[28] Kim, J., Keller, J., and Kumar, V., "Design and Verification of Controllers for Airships," *Proceedings of the International Conference on Intelligent Robots and Systems*, IEEE, Las Vegas, Nevada, USA, 2003.

[29] Moutinho, A. and Azinheira, J. R., "Path Control of an Autonomous Airship Using Dynamic Inversion," *Proceedings of the 5th IFAC/EURON Symposium on Intelligent Autonomous Vehicles*, Lisbon, Portugal, 2004.

[30] Yan, Z., Weidong, Q., Yugeng, X., and Zili, C., "Stabilization and Trajectory Tracking of Autonomous Airships Planar Motion," *Journal of Systems Engineering and Electronics*, Vol. 19, 2008, pp. 974–981.

[31] Repoulias, F. Papadopoulos, E., "Robotic Airship Trajectory Tracking Control Using a Backstepping Methodology," *Proceedings of the International Conference on Robotics and Automation*, IEEE, Pasadena, CA, USA, 2008.

[32] Melbous, A., Tami, Y., Guessoum, A., and M., H., "UAV Controller Design and Analysis Using Sliding Mode Control," *Journal of Automation and Systems Engineering*, Vol. 4, No. 2, 2010.

[33] Avenant, G., "Autonomous Flight Control System for an Airship," Master of Science Thesis, Stellenbosch University, Stellenbosch, South Africa, 2010.

[34] Dorato, P., Abdallah, C., and Cerone, V., *Linear-Quadratic Control: An Introduction*, Prentice Hall Inc., Englewood Cliffs, New Jersey, 1995.

[35] Masar, I. and Stohr, E., "Gain Scheduled LQR Control for an Autonomous Airship," *18th International Conference on Process Control*, Tatranska Lomnica, Slovakia, 2011.

[36] Nakpiam, J., "Control of Airship Motion in Presence of Wind," MS thesis, Department of Mechanical and Aerospace Engineering, The University of Texas at Arlington, Arlington, Texas, USA, 2011.

[37] O.I.Elgerd, *Control Systems Theory*, McGraw-Hill, 1966.

[38] Franklin, G. F., Powell, J. D., and Emami-Naeini, A., *Feedback Control Systems*, Prentice-Hall, 2002.

[39] Oral, O., Cetin, L., and Uyar, E., "A Novel Method on Selection of Q And R Matrices In The Theory Of Optimal Control," *International Journal of Systems Control*, Vol. 1, No. 2, 2010, pp. 84–92.

[40] A. E. Bryson, J. and Ho, Y.-C., *Applied Optimal Control*, USA: Hemisphere Publishing Corporation, 1975.

[41] Shukla, U. and P., M., "The Proportional Navigation Delemma - Pure or True?" *IEE Transactions on Aerospace and Electronic Systems*, Vol. 26, No. 2, 1990, pp. 382–392.

[42] Lu, P., "Intercept of Nonmoving Targets at Arbitrary Time-Varying Velocity," *Journal of Guidance, Control, and Dynamics*, Vol. 21, No. 1, 1998, pp. 176–178.

[43] Han, S.-C., Bang, H., and Yoo, C.-S., "Proportional Navigation-Based Collision Avoidance for UAVs," *International Journal Of Control Automation And Systems*, Vol. 7, No. 4, 2009, pp. 553–565.

[44] Athans, M., "The Importance of Kalman Filtering Methods for Economic Systems," *Annals of Economic and Social Measurement*, Vol. 3, No. 1, 1974, pp. 49–64.

[45] Fleury, A., Trigo, F., and Martins, F., "Application of Computer Vision and Kalman Filtering Techniques to Identify Oil Flames Nebulization Quality," *ABCM Symposium Series in Mechatronics*, Vol. 4, 2010, pp. 1–10.

[46] Gao, J., Kosaka, A., and Kak, A., "A multi-Kalman filtering approach for video tracking of human-delineated objects in cluttered environments," *Computer Vision and Image Understanding*, Vol. 102, 2006, pp. 260–316.

[47] Campbell, M. and Brunke, S., "Nonlinear Estimation of Aircraft Models for On-Line Control Customization," *Proceedings of the Aerospace Conference*, IEEE, Big Sky, MT, USA, 2001.

[48] Kallapur, A. and Anavatti, S., "UAV Linear and Nonlinear Estimation Using Extended Kalman Filter," *Proceedings of the Computational Intelligence for Modeling, Control and Automation*, IEEE, Sydney, NSW, Australia, 2006.

[49] Langelaan, J. W., "State Estimation for Autonomous Flight in Cluttered Environments," *Journal of Guidancs, Control, and Dynamics*, Vol. 30, No. 5, 2007, pp. 1414–1426.

[50] Grillo, C. and Vitrano, F. P., "State Estimation of a Nonlinear Unmanned Aerial Vehicle Model using an Extended Kalman Filter," *Proceedings of the 15th International Space Planes and Hypersonic Systems and Technologies Conference*, AIAA, Dayton, Ohio, USA, 2008.

[51] Lievens, K., "Single GPS Antenna Attitude Determination of a Fixed Wing Aircraft Aided with Aircraft Aerodynamics," MS Thesis, Faculty of Aerospace Engineering, Delft University of Technology, Delft, Netherlands, 2004.

[52] Jose, J. M., "Performance comparison of Extended and Unscented Kalman Filter implementation in INS-GPS integration," Master Thesis, Department of Space Science,Lulea University of Technology, Lulea, Sweden, 2009.

[53] Petrich, J. and Subbarao, K., "On-Board Wind Speed Estimation for UAVs," *Proceedings of the Guidance, Navigation, and Control Conference*, AIAA, Portland, Oregon, USA, 2011.

[54] Veld, A., de Jong, P., van Paassen, M., and Mulder, M., "Real-time Wind Profile Estimation using Airborne Sensors," *Proceedings of the Guidance, Navigation, and Control Conference*, AIAA, Portland, Oregon, USA, 2011.

[55] Langelaan, J. W., "Wind Field Estimation for Small Unmanned Aerial Vehicles," *Journal of Guidancs, Control, and Dynamics*, Vol. 34, No. 4, 2011, pp. 10161030.

[56] Patino, D., Solaque, L., Lacroix, S., and Gauthier, A., "Estimation of the Aerodynamical Parameters of an Experimental Airship," *Proceedings of theRobot Vision for Space Applications Conference*, IEEE/RSJ IROS, Alberta, Canada, 2005.

[57] Bijker, J., "Development of an Attitude Heading Reference System for an Airship," M.S Thesis, Department of Electrical and Electronic Engineering, the University of Stellenbosch, Stellenbosch, South Africa, 2206.

[58] Bijker, J. and Steyn., W., "Kalman Filter Configurations for a Low-cost Loosely Integrated Inertial Navigation System on an Airship," *Control Engineering Practice*, Vol. 16, No. 12, 2008, pp. 15091518.

[59] Crassidis, J. L., , and Junkins., J. L., *Optimal Estimation of Dynamic Systems*, CRC Press, 2004.

BIOGRAPHICAL STATEMENT

Ghassan M.Atmeh was born in Amman, Jordan, in 1987. He received his B.S. degree in Mechanical Engineering with an Aeronautics major from the Jordan University of Science and Technology, Irbid, Jordan, in 2010. During his undergraduate studies he interned at the Jordan Aeronautical-Systems Company and the Royal Jordanian Air force. He then moved to the US in July of 2010 to acquire his M.S. degree in Aerospace Engineering from The University of Texas at Arlington where he specialized in linear and nonlinear systems analysis and control. His current research interests are autonomous vehicles control, estimation theory, nonlinear systems analysis, nonlinear control and structural health monitoring. He is also a student member of AIAA and ASME.